



Published in final edited form as:

Annu Rev Biochem. 2020 June 20; 89: 45–75. doi:10.1146/annurev-biochem-013118-111843.

Ribonucleotide Reductases (RNRs): Structure, chemistry, and metabolism suggest new therapeutic targets

Brandon L. Greene^{1,2,3}, Gyunghoon Kang², Chang Cui^{2,3}, Marina Bennati^{4,5}, Daniel G. Nocera³, Catherine L. Drennan^{2,6,7}, JoAnne Stubbe^{2,6}

¹Department of Chemistry and Biochemistry, University of California Santa Barbara, Santa Barbara, California 93106

²Department of Chemistry, Massachusetts Institute of Technology, Cambridge, Massachusetts 02139;

³Department of Chemistry and Chemical Biology, Harvard University, Cambridge, Massachusetts 02138;

⁴Max Planck Institute for Biophysical Chemistry, 37077 Göttingen Germany

⁵Department of Biophysical Chemistry, University of Göttingen, Göttingen Germany

⁶Department of Biology, Massachusetts Institute of Technology, Cambridge, Massachusetts 02139

⁷Howard Hughes Medical Institute, Massachusetts Institute of Technology, Cambridge, Massachusetts 02139

Abstract

Ribonucleotide reductases (RNRs) catalyze the de novo conversion of nucleotides to deoxynucleotides in all organisms, controlling their relative ratios and abundance and in doing so play an important role in fidelity of DNA replication and repair. RNR's central role in nucleic acid metabolism has resulted in five therapeutics that inhibit human RNR. In this review we discuss the structural, dynamic, and mechanistic aspects of RNR activity and regulation, primarily for the human and *E. coli* class Ia enzymes. The unusual radical-based organic chemistry of nucleotide reduction, the inorganic chemistry of the essential metallo-cofactor biosynthesis/maintenance, the transport of a radical over a long distance and the dynamics of subunit interactions all present distinct entry points toward RNR inhibition relevant for drug discovery. Our current mechanistic understanding of small molecules that target different elements of RNR function are described, including downstream pathways that lead to cell cytotoxicity. We conclude by summarizing novel and emergent RNR targeting motifs for cancer and antibiotic therapeutics.

Keywords

ribonucleotide reductases; structures; mechanisms; therapeutics

Introduction.

The availability of adequate and balanced deoxynucleotide pools is essential for accurate DNA replication and repair and consequently genome stability. Deoxynucleotides are supplied universally in all organisms by a *de novo* pathway catalyzed by ribonucleotide reductases (RNRs) that convert RNA building blocks to DNA building blocks (1–3). Deoxynucleotides can also be generated in an organism-, environment-, and disease-specific fashion by nucleoside (or nucleotide) salvage pathways (4). Our current understanding of the unique organic (5) and inorganic chemistry (6) of RNRs, have been revealed, in part, by our understanding of clinically used therapeutics that target the universal radical-mediated nucleotide reduction mechanism, and the specific metallo-cofactor biosynthetic and repair pathways. The ensemble of studies led to the first structures of class I RNRs at low resolution (7–10), and more recently, to high resolution structures in trapped active and inhibited states (8, 11, 12). These new studies suggest, in combination with inhibitors of specific signaling pathways downstream of RNR, that the time is right to revisit RNR as a target for antibacterial, antiviral, as well as anticancer agents.

All RNRs catalyze the conversion of nucleoside diphosphates (NDPs) or triphosphates (NTPs) to deoxynucleotides (dNDP or dNTP, Figure 1A). The RNR's share a common active site architecture located in subunit α that houses 3 essential cysteines (Figure 1B) (13–15). Two cysteines (bottom face) provide the reducing equivalents to make dNDPs and the third cysteine (top face) is transiently oxidized to a thiyl radical ($-S\bullet$) that initiates NDP reduction (16). Distinct metallo-cofactors catalyze this oxidation (Figure 1C) and they are the main basis for RNR classification (Ia-e, II, III), though a recently discovered non-metallo-cofactor, 2,3-dihydroxyphenylalanine radical (DOPA \bullet) breaks this paradigm (17–19). This review focuses on the class I RNRs that share a distinct mechanism by which a transient thiyl radical is generated, and whose formation requires a second subunit β that houses the cofactor oxidant (Figure 1C).

Docking model and Radical Transfer (RT) pathway.

Reichard and coworkers in 1969 discovered the class Ia *E. coli* RNR and proposed that active enzyme is an $\alpha_2\beta_2$ complex (20, 21). However, it wasn't until 1994 that Eklund et al. (13) reported the X-ray structure of α_2 (Figure 2B), which together with their earlier structure of β_2 (Figure 2A) led to a symmetrical “docking model” based on subunit shape complementarity (Figure 2C). This model has guided experimentation until recently. A fascinating feature of the docking model is that the diferric-tyrosyl radical cofactor (Fe^{3+}_2 -Y₁₂₂ \bullet , Figure 2C) in β is ~ 35 Å away from C₄₃₉ (*E. coli* numbering), which is oxidized in the α subunit. A turnover frequency for dNDP production of 2 to 10 s⁻¹, together with the long distance between Y₁₂₂ \bullet and C₄₃₉, engender a RT pathway (7, 14): Y₁₂₂ \bullet [β] \rightleftharpoons [W₄₈[β]] \rightleftharpoons Y₃₅₆[β] to Y₇₃₁[α] \rightleftharpoons Y₇₃₀[α] \rightleftharpoons C₄₃₉[α] (Figure 3, noting that [W₄₈] involvement has not yet been demonstrated).

Rate limiting physical step(s) mask both the NDP reduction and the RT chemistry. These processes are conformationally gated by proper substrate and effector binding to α_2 and its association with β_2 (22). The “stable” Y₁₂₂ \bullet in β is transiently reduced and re-oxidized on each turnover, and RT through the pathway involves distinct proton-coupled electron transfer

(PCET) steps at each pathway residue (Figure 3). The first step in RT is proposed to occur at the metal cofactor in $\beta 2$, triggered by substrate and effector binding in $\alpha 2$ more than 35–40 Å away. Studies using site-specifically incorporated tyrosine analogs with altered reduction potentials, high field, multifrequency, electron paramagnetic resonance (EPR) methods, structural analysis, and RT photoinitiation in photosensitized RNRs (photo-RNRs) have provided insight into each of the proposed steps (7). Our current understanding of this pathway suggests that the thermodynamic landscape of the radical transfer process (Y_{122}^{\bullet} to C_{439}) is uphill by greater than 200 mV, and that the NDP reduction reaction, which also involves an uphill 3'-hydrogen atom abstraction, is driven to the right by rapid and irreversible loss of water during NDP reduction (Figure 1A). This pathway design avoids buildup of the highly reactive protein radical intermediates such as Y^{\bullet} , which has a reduction potential of 0.96 V vs the normal hydrogen electrode). Reduction of any of the Y^{\bullet} intermediates in the pathway (Figure 3) would inactivate RNR ending in catastrophic consequences for the organism (23, 24). Accordingly, the RT pathway provides a target of opportunity for future drug design.

Evidence for the docking model (Figure 2C) has been provided by trapping pathway radicals using tyrosine analogs with perturbed reduction potentials (Figures 3 and 4A), and active site radicals in $\alpha 2$ using MBIs (Figure 4B) (25). As briefly summarized, pulsed electron-electron double resonance (PELDOR) spectroscopy and negative stain electron microscopy (EM) have allowed spectroscopic analysis of these trapped $\alpha 2\beta 2$ complexes.

3-Aminotyrosine (NH_2Y)-RNR (Figure 4) and PELDOR analysis: low resolution evidence for the docking model.

NH_2Y is easier to oxidize than Y by 590 mV (Figure 4A). When NH_2Y replaces a pathway Y in α or β and is incubated with the second subunit, substrate, and specificity effector, it functions as an efficient radical trap forming a 3-aminotyrosyl radical (NH_2Y^{\bullet}) (10, 25) that is unable to oxidize the next residue in the pathway. Under these conditions, 0.5 equivalents of total Y_{122}^{\bullet} in $\beta 2$ is reduced and a stoichiometric amount of NH_2Y^{\bullet} is formed in (α/β pair, one side). Because the chemistry in one α/β pair is incomplete, 0.5 equivalents of Y_{122}^{\bullet} resides in the adjacent α/β pair (on the other side), which is unable to carry out chemistry. These results require asymmetry within $\alpha 2\beta 2$ and are described as half-sites reactivity.

In these trapped complexes, PELDOR spectroscopy has been used to measure the distance between the NH_2Y^{\bullet} (located at 356- β or 731- α or 730- α) in one α/β pair and the Y_{122}^{\bullet} on the adjacent pair, as shown in Figure 5A. Studies with the MBI N_3CDP (Figure 4B), which forms a nitrogen centered radical (N^{\bullet}) covalently bound to a cysteine in the active site of $\alpha 2$, also allows a distance measurement. Additionally, RNR mutants in which Y_{122}^{\bullet} is replaced with 2,3,5- F_3 - Y_{122}^{\bullet} or $NO_2Y_{122}^{\bullet}$ (Figure 4A), which are “hotter” oxidants than Y_{122}^{\bullet} , also generate pathway radicals and demonstrate half-site reactivity (26). Distances measured to date are summarized in Table 1 and they are consistent with the docking model (Figure 2C) (25, 26). An unexpected outcome of these experiments was that when radicals are trapped within the pathway, the $\alpha 2\beta 2$ complex exhibits increased subunit affinity, thus enabling its isolation. A number of these complexes have been examined by negative stain EM and have revealed structures resembling the docking complex (15–30 Å resolution (Figure 5B) (7).

Our current model from these studies with perturbants is that for wild type RNR, radical transfer and catalysis occur initially within one α/β pair of an asymmetric $\alpha_2\beta_2$, which triggers rapid chemistry within the second α/β pair. The mechanism of switching remains to be determined.

Higher resolution structures of RNRs

Inhibited structures *in vitro*.

dATP is a universal inhibitor of all class Ia RNRs. It binds to the N-terminal domain of α (cone domain, green, Figure 2B). Two independent studies by the Dealwis and Walt groups (2011) (8) and Drennan and Asturias groups (2018) (27) revealed structures of eukaryotic dATP-inhibited states. Fairman et al studying *S. cerevisiae* RNR observed crystallographically, an α_6 hexameric ring structure (6.6 Å). Brignole et al studying human α with CDP, dATP and a small amount of ATP, observed by cryo-EM, a similar, but higher resolution hexameric ring structure (Figure 6B, 3.3Å). Both groups also reported negative stain EM studies (28 and 30 Å) (8, 27) of a dATP inhibited state in the presence of both α and β (1:1). Despite the stoichiometry of the subunits, in both cases, less than 1 β_2/α_6 was observed. Both eukaryotic dATP inhibited states are a trimer of dimers with the cone domains responsible for the dimer interfaces. In addition, with the human RNR, small-angle X-ray scattering data on this state suggested that β_2 could not enter the hole in the α_6 ring structure, and hence that an active $\alpha_2\beta_2$ is not accessible (28).

The structure of the dATP inhibited *E. coli* Ia RNR generated from $\alpha:\beta$ (1:1) in the presence of dATP is distinct from its eukaryotic counterparts. Drennan and collaborators using a variety of biophysical methods, reported an $\alpha_4\beta_4$ ring complex with alternating α_2 and β_2 s and a hole in the center (Figure 6A) (29, 30). In this structure, in contrast with the eukaryotic inhibited state, the cone domain (green) interacts with β_2 . The most intriguing result is that the distance between Y₁₂₂- β_2 and C₄₃₉ in α_2 (Figure 2C) has increased from 35 to 60 Å, shutting down radical transfer and consequently nucleotide reduction. Thus, despite the distinct quaternary structures of the dATP-inhibited states, a common mechanism of inhibition emerges that involves inability of β_2 to form an active $\alpha_2\beta_2$ state.

Inhibited structures *in vivo*.

The presence of these inhibited states in cells (Figure 6) are important to establish. Drennan et al. used their structural insight from the *E. coli* $\alpha_4\beta_4$ complex and site-directed mutagenesis to disrupt the α_2 -cone domain- β_2 interface. Activity assays and negative stain EM analysis of several mutants showed that dATP no longer inhibited RNR and, that no $\alpha_4\beta_4$ was detected (31). This study, in concert with genetic experiments on *E. coli* using a random mutagenesis protocol, a screen for altered dNTP pools, and genome sequencing, identified RNR with mutations at the same interface (32). The biochemical and genetic studies together suggest that the dATP-inhibited state of *E. coli* $\alpha_4\beta_4$ occurs *in vivo*. Studies with clofarabine (CIF) (33) and other nucleoside therapeutic (cladribine (CIA) and fludarabine (FIU)) inhibitors of RNR (Figure 4B) (34) have demonstrated α_6 formation in several human cell lines treated with sublethal doses of the nucleosides (35). The distinct

inhibitory structures of the Ia RNRs (Figure 6) will be discussed further in the section on mechanism-based and reversible inhibitors as a new strategy to target RNRs.

Toward Active $\alpha\beta$ structures.

Our studies using fluorinated tyrosine analogs (Figure 4A) combined with bioinformatics and the docking model of $\alpha\beta$ (Figure 2C) to identify residues within the α/β subunit interface including E52 in β , led us to investigate the *E. coli* double mutant of β (E52Q and F₃Y₁₂₂•) (11). The F₃Y₁₂₂ substitution allowed trapping of the Y₃₅₆• on the RT pathway (Figure 3) resulted in a tighter subunit affinity, $K_d < 0.4$ nM as compared with 0.2 μ M for the control with E52Q- β (36). Although E52Q- β when incubated with any substrate and effector resulted in completely inactive RNR, incubation of the double mutant β (E52Q and F₃Y₁₂₂•) with α 2 (or His₆- α 2), GDP, and TTP produced 0.5 equivalents of Y₃₅₆• and 0.5 equivalents of dGDP consistent with half-sites reactivity (36). The resulting α 2(E52Q and F₃Y₁₂₂• β 2) complex gave rise to a near atomic resolution (3.3 to 5 Å) cryo-EM structure shown in Figure 2D which is asymmetric, consistent with the half-sites reactivity. In line with the biochemistry, the structure of α (left, Figure 2D) has generated a disulfide in the active site that we presume gives rise to the dGDP. With the α/β pair on the right side of the complex in Figure 2D, residues 341–375 in β are visualized for the first time (Figure 2A). In addition, GDP/TTP are apparent and the location of Y₃₅₆ is finally revealed for the first time as part of the entire radical transfer pathway (Figures 2C and 3) (11). The details of this structure have recently been submitted for publication. Our ability to trap radicals at different residues within the pathway summarized in Table 1 and the increased subunit affinity observed under these conditions, suggests that this approach may lead to additional cryo-EM structures that will provide insight about the dynamics of this amazing machine.

New mechanistic insight about the chemistry of NDP reduction

Model for disulfide re-reduction and conformational gating.

In the *E. coli* RNR, the rate-limiting step(s) are physical (Figure 7 step B, E and G), involving conformational changes that mask the chemistry of long-range reversible RT and dNDP formation (22, 37). The observed rate constants (k_{cat}) for dNDP formation in the absence of an external reductant (steps A through E), range from 2 to 5–10 s⁻¹ with substrate and substrate/effector, respectively. In the presence of the physiological reductants (in cells or in steady state assays), additional conformational changes become rate limiting (1–2 s⁻¹, step H) and likely involve either α/β subunit dissociation, conformational changes associated with the re-reduction of the active site disulfide by the C-terminal tail of α (steps F, G, H), or both, and are protein concentration dependent. Different α s have distinct cysteine configurations within their C-terminal tails (red balls in the C-terminal tails in Figure 2B) and require organism-specific reductants (e.g. thioredoxin (TR), NrdH, glutaredoxin (Grx), and thioredoxin reductase (TRR) and glutaredoxin reductase) (38–41).

To unmask the mechanistic details of dNDP formation, multiple methods have been employed including site-directed mutagenesis, insertion of unnatural amino acids (Figure 4A), photosensitized RNRs (photo- β 2), and MBIs (Figure 4B). In subsequent sections, we

describe how this information combined with structural studies have provided insight into new therapeutic strategies.

NDP reduction mechanism.

Our current mechanism for nucleotide reduction is shown in Figure 8 (5, 43). The important features are that a $-S\cdot$ (C_{439} , *E. coli*) initiates the reduction by removal of the NDP 3'-H (step A) (44). E_{441} facilitates this step by functioning as a base catalyst for 3'-OH deprotonation (1 to 2) (45). This reaction is driven to the right by the rapid, irreversible loss of water catalyzed by C_{225} (step B). The proposal for the reductive half-reaction (steps C and D) is that the 3'-keto-2'-radical [3] is reduced by PCET to generate the 3'-ketodeoxynucleotide and the three electron, disulfide radical anion [4]. This species then reduces the 3'-ketone by another PCET step (step D) where the proton is supplied by the protonated E_{441} . In the last step, the H-atom abstracted from the 3' position of NDP is returned to the same position to form dNDP and the $C_{439}\cdot$, that reoxidizes Y_{122} in $\beta 2$ on each turnover.

Role of multiple thiyl radicals.—The role of the $-S\cdot$ initiator (C_{439} , Figure 8) was previously established based on studies with the class II, adenosylcobalamin-dependent ribonucleotide triphosphate reductase. An exchange coupled $-S\cdot$ -cob(II)alamin species, detected by EPR and UV-vis absorption stopped flow spectroscopies, was shown to be chemically and kinetically competent in deoxynucleotide formation (46, 47). The structural homology and conserved residues in the active site of all RNRs (Figure 1B) have thus been used to infer the universal involvement of $-S\cdot$ in initiating 3'-H atom abstraction (16). Support for $-S\cdot$ involvement in the reductive half-reaction (Figure 8 step C and D) comes from studies with $E_{441}Q$ - α/β /CDP/TTP where a disulfide radical anion was spectroscopically identified due to the absence of a required proton from E_{441} for the PCET step D (48). Although $-S\cdot$ chemistry has been proposed for many enzymatic reactions, RNR is the only enzymatic system where this intermediate has been detected (46, 47).

PhotoRNRs unmask rate constants for NDP reduction chemistry.—The development of methods to uncouple conformational gating and unmask chemistry has allowed unprecedented insight into the active site chemistry, including thiyl radical mediated hydrogen atom abstraction (Figure 8, step A) (49, 50) and the subsequent rate-limiting 3'-ketodeoxynucleotide reduction (step D, 4 to 5) (23,26). In the former case, we designed a method for photosensitization of RNR (Figure 9A) in which a photooxidant, bromomethylpyridyl rhenium(I) tricarbonyl phenanthroline ([Re]), is covalently attached to a single surface-exposed cysteine in $S_{355}C$ - $\beta 2$ mutant; the $Y_{122}\cdot$ in $\beta 2$ is reduced and Y_{356} in $\beta 2$ is replaced with a fluorinated tyrosine ($F_n Y_{356}$, Figure 4A). This photo $\beta 2$ in complex with $\alpha 2$, substrate, and effector, can be rapidly (ns) oxidized to a $F_n Y_{356}\cdot$ - $\beta 2$ state upon illumination (Figure 9B). The photochemically generated radical rapidly equilibrates with the radical transfer pathway in $\alpha 2$, ultimately oxidizing C_{439} , initiating cleavage of the 3' C-H bond of NDP. Comparison of the $F_n Y_{356}\cdot$ decay, observed by transient absorption spectroscopy, in the presence of 3'-[$^{1(2)}H$]-CDP established a lower limit for the $-S\cdot$ mediated H-atom abstraction (step A) of $1.3 \times 10^4 \text{ s}^{-1}$ and an isotope effect of 7 (51)! Note

that the k_{cat} for RNR is 2–10 s^{-1} . The RT chemistry is thus very fast (!) and unmasked for the first time using this method.

The subsequent rate-limiting 3'-ketodeoxynucleotide reduction (step D, Figure 8) has been examined by incorporating tyrosine analogs with altered reduction potentials in place of Y₁₂₂ in β . Use of these “hotter” oxidants drives radical transfer and also uncouples conformational gating. Specifically, F₃Y₁₂₂• and NO₂Y₁₂₂• (*vide supra*) have higher reduction potentials than the native Y₁₂₂•(β 2) by 80 and >200 mV, respectively (23, 26), as determined from the independent measurements of formal reduction potentials in the small 3-helix bundle protein (24). These β 2 mutants have been studied in an effort to observe the slow step(s) within the proposed chemistry, specifically the PCET reduction of the 3'-ketone by the disulfide radical anion (Figure 8, 4 to 5, step D). When NO₂Y₁₂₂•- β 2 (or F₃Y₁₂₂•- β 2) is mixed with α 2/CDP/ATP, dCDP formation occurred at \sim 150 s^{-1} (30 s^{-1}). This rate constant is similar to the 50 s^{-1} measured for dCTP formation; the latter is catalyzed by class II RNR (52) where the active site chemistry is not masked by physical steps and is much faster than the wt turnover of 1–2 s^{-1} .

MBIs and reversible inhibitors to understand mechanism and design of new therapeutics.

The MBIs 2'-halo (X)-2'-deoxyNDPs (XNDP, X = Cl, F; Figures 4B irreversible and Figure 10) have played a pivotal role in our current understanding of the mechanism of nucleotide reduction (53). In 1976 Thelander and Eckstein et al. reported that ClCDP incubated with *E. coli* RNR resulted in time-dependent release of Cl⁻ and cytosine, and that the α subunit was inactivated (54). These observations provided the impetus for studies using labeled nucleotide analogs, which led to the general model for inhibition shown in Figure 10. As with the NDP substrate, the -S• abstracts the 3'-H (step A) to generate **2**. The outcome of the reaction depends on whether and how the loss of X at 2'-C is catalyzed by the enzyme. From **3**, the 2'-delocalized radical can be reduced from the top face by H-atom transfer mediated by C₄₃₉ (red H) or the bottom face (blue H) facilitated by C₂₂₅. With Cl(F)NDP, a 3'-ketodeoxynucleotide is generated (**7**) that dissociates from the active site (when X is not protonated). Intermediate **7** can decompose on a minute time scale to nucleic acid base, pyrophosphate (PP_i), and a furanone (**8**) that non-specifically alkylates the α subunit. If the reduction of **3** is by C₄₃₉, then reverse RT can effectively regenerate the Y₁₂₂• in β 2. However, if reduction occurs from the bottom face, Y₁₂₂ remains reduced and β 2 is inactivated. Thus, α and/or β can be inactivated via distinct mechanisms. With both XNDPs (X = Cl, F), if X is protonated (XH, step B above arrow), then dNDP is formed. The details of RNR inactivation *in vitro* and *in vivo* depend on the identities of substrate and effector, leaving group (X), and the reductant. In all cases, α inactivation requires Y₁₂₂• reduction. These inhibitors inactivate class I, II, and III RNRs by a common mechanism suggesting similar active sites (Figure 1B). The involvement of the α C-terminal cysteines in enzyme inhibition (Figure 2B, red balls) is not well understood as their covalent linkage to **8** is reversible, precluding isolation and characterization of alkylated α .

In contrast to XNDPs ($X = \text{Cl}, \text{F}$), there are a number of MBIs ($X = \text{N}_3, \text{F}_2, \text{VF}$, Figure 4B) (55–57) that share similar chemistry in steps **A** and **B** (Figure 10), but then undergo distinct chemistry controlled by X and the active site cavity. Unraveling the mechanism by which N_3NDP inactivates all RNRs defined the strategy to study the mechanism of action of the clinically used nucleoside therapeutics, gemcitabine (F_2C) and clofarabine (CIF). F_2CDP is an irreversible inhibitor (58) and, in contrast to expectations, CIFDP and CIFTP are reversible, non-covalent inhibitors (Figure 4B) (59–61).

2'-Azido-2'-deoxynucleotide (N_3NDP).

N_3NDPs ($\text{N} = \text{C}$ (shown in Figure 4B), U or A) are substoichiometric MBIs that were also first reported by Thelander and Eckstein (54). Extensive studies with N_3UDP revealed that its incubation with $\alpha 2\beta 2$ resulted in rapid loss of ~90% RNR activity concomitant with loss of only 0.5 equivalents of $\text{Y}_{122}\bullet$. The $\text{Y}\bullet$ loss was biphasic with the fast phase accompanied by formation of a nucleotide-based nitrogen centered radical ($\text{N}\bullet$) derived from the N_3 moiety that was structurally identified using isotopically labeled N_3UDPs and EPR methods (Figure 11) (62, 63). The $\text{N}\bullet$ species then slowly decomposes to form nucleoside base (blue N in Figure 11), PP_i , and **8**. The α/β subunits dissociate, and subsequent to $\alpha 2\beta 2$ complex reformation, more $\text{Y}\bullet$ is lost and $\text{N}\bullet$ formed. While these observations were perplexing at the time, the many recent examples of “half-site” reactivity (Table 1) and RNR asymmetry (Figure 2D), now place these observations on firm footing.

In vitro N_3CDP inhibits $\beta 2$ by reduction of the essential $\text{Y}_{122}\bullet$ whereas *in vivo*, the nucleoside analog N_3C is not cytotoxic. In cells, N_3C is not readily phosphorylated to N_3CMP by deoxycytidine kinase, presaging the importance of the specificity of kinases in generation nucleotide (di and triphosphate) therapeutics.

Gemcitabine (F_2C) and clofarabine (CIF), clinically used nucleoside therapeutics that inhibit human RNR.

F_2C and CIF are used clinically as cancer therapeutics (Figure 4B). F_2C targets a broad spectrum of solid tumors (pancreatic, metastatic breast, lung) and hematological cancers. In the clinic, this compound is used in combination with DNA damaging agents such as cisplatin or small molecule inhibitors of signaling pathways that affect the cells response to DNA replication stress (3, 64–66). CIF is limited to hematological cancers (AML, ALL). Both agents inhibit DNA synthesis. RNR is the upstream target of the diphosphate forms of these compounds (F_2CDP , CIFDP), whose inhibition alters dNTP pools. Additionally, the triphosphate forms of these compounds (F_2CTP , CIFTP) inhibit DNA polymerases by incorporation into DNA. The mechanisms, however, by which these compounds inhibit RNR and DNA synthesis, are distinct.

F_2CDP .

F_2C was synthesized independently by research groups at Merrill Dow and Lilly (58, 67). Studies from Plunkett and the Lilly group demonstrated that F_2C inhibited growth of a variety of tumor cell lines and that the cytotoxicity resulted from inhibition of multiple targets including DNA polymerases and RNR (67–69). Biochemical studies on *E. coli* and human RNR established that F_2CDP is a time-dependent irreversible inhibitor and that

inactivation occurs with one equivalent per α_2 subunit. Studies using isotopically labeled F_2CDPs established that the products of the inactivation were distinct depending on whether they were carried out in the presence or in the absence of reductant (70–72).

In the presence of reductant (TR/TRR or DTT), $2F^-$, cytosine, PP_1 and one alkylated α -cysteine (C_{225}) per α_2 were identified and no $Y_{122}\bullet$ in β_2 was lost. Under these conditions, while only 0.5 equivalents of α is inactivated and β remains active, all enzymatic activity is lost. Analysis of the inhibited reaction mixture by SDS-PAGE with no heating revealed that α migrated as a 60:40 ratio of 80 kDa (endogenous α molecular weight) to 110 kDa (modified α) (Figure 12A and B). In cancer cell lines incubated with F_2C , SDS PAGE analysis of cell lysate revealed that the α subunit also migrated in a 60:40 ratio (Figure 12B), similar to the *in vitro* studies (73). Similar experiments in the absence of reductant, resulted in 50% loss of the β_2 - $Y_{122}\bullet$ and formation of an equivalent amount of a new, nucleotide-based radical (structure shown in Figure 12C). This radical slowly breaks down to cytosine and PP_1 . Inhibition was accompanied by loss of $2F^-$, but the α subunit was not covalently labeled. Thus, both in the presence and absence of reductant, 1 F_2CDP/α_2 is sufficient for inhibition, although the underlying mechanisms of inactivation are distinct.

To account for the complete inactivation of RNR with only 0.5 equivalents F_2CDP/α , we proposed that the α/β subunit affinity increased and switching to the second α/β pair for additional chemistry is prevented. To test this possibility, inactivated *E. coli* and human RNR were subjected to size exclusion chromatography (SEC) analysis. The former showed a species consistent with an apparent molecular weight for $\alpha_2\beta_2$ and the latter with $\alpha_6\beta_6$ (74). In the control, in the absence of F_2CDP , the subunits separate with β eluting as a dimer and α as a mixture of monomers and dimers consistent with weak subunit interactions. Based on our recent EM analyses of a mixture of α and β (1:1) with CIFTP (Figure 6C and the next section) (27), the size with human-RNR attributed to $\alpha_6\beta_6$ is not possible. Altered molecular weights using SEC analysis can be attributed to unusual, non-globular, shapes ($\alpha_6\beta_2$) or altered quaternary structure(s). Fibril structures for example have been reported with human α and ATP (27) and with *Bacillus subtilis* class Ib (α/β) RNR (75).

CIFDP and CIFTP (reversible).

Early studies by Plunkett et al. established the toxicity of CIF towards many cell lines (CEM, K562, Hep2). In cell-free systems, CIFTP inhibits RNR and DNA polymerase α and ϵ (59, 60, 66, 76). The observation that the CIFTP:CIFDP ratio in some cells was 7:1, led to the proposal that CIFTP was a reversible inhibitor of ATP binding to the A-site of α (Figure 2B, cone domain (green)). To better understand how RNR is targeted, kinetic and biochemical studies were undertaken with both CIFDP and CIFTP (61). CIFDP was shown to be a reversible, time-dependent, slow binding, inhibitor to the C-site. The kinetic analysis revealed a two-step binding mechanism with a K_1^* of 17 nM. CIFTP exhibits reversible, time-independent A-site binding. With CIFTP in 5-fold excess relative to RNR under physiological conditions, RNR activity was rapidly and completely lost with a K_1 of 40 nM. With sample dilution and follow-up assays, enzyme activity was recovered over 30 min but only to 50% of the initial value. The $t_{1/2}$ of the human $Y\bullet$ in β_2 is 30 min at 37 °C (61) and the α subunit is prone to oxidation, making the kinetic measurements challenging; further

studies are required. To determine if the observed inhibition was associated with changes in RNR's quaternary structure, studies of CIFTP (CIFDP) with α , with and without allosteric effector (dGTP), were each examined by SEC. In the absence of the corresponding nucleotide in the elution buffer, α migrated as α_6 in the presence of either CIFTP and CIFDP. This result is distinct from dATP- α_6 . When dATP is absent from the elution buffer during SEC, the hexamer rapidly reverts to α monomer. Thus, the presence of CIFDP or CIFTP alters α 's quaternary structure such that, even subsequent to CIFD(T)P dissociation, α_6 remains trapped in the inactive state! β_2 had no effect on the inhibition or migration on SEC analysis. Structures of CIFTP mixed with human α/β (1:1) were examined by cryo-EM and solved to 30-Å resolution (Figure 6C). Less than 1 β_2 per 3 α_2 was observed and it appeared randomly positioned on the exterior or on top of a hexameric ring structure (Figure 6C) (27). In support of this model, experiments with D57N- α , where the mutation in the cone domain prevents hexamerization of α , revealed that neither CIFD(T)P treated mutant-RNR, nor CIF treated cells with mutant RNR were inhibited. Finally, *E. coli* RNR, which does not form α_6 structures, is not inhibited by CIFDP (61).

The dynamics of quaternary structure interconversions offer an opportunity to inhibit RNRs through unconventional mechanisms. The flexible cone domains (Figure 2, Figure 6A and B) (27, 30) play critical, but distinct roles in these states. Strengthening or weakening the interactions responsible for these quaternary structures with small molecules could alter RNR activity.

To assess the importance of the hexameric state of human-RNR, studies were carried out with His₆- α expressed at 3 or 30 \times endogenous levels in COS cells that were then treated with noncytotoxic levels of CIF for 3 h. Analysis of the 30 \times material purified by Ni-affinity chromatography revealed the α_6 state was present; with 3 \times endogenous levels crosslinking was required to detect α_6 . The α_6 state from these and other studies is likely the inhibited state inside the cell in the presence of CIFTP and dATP (33).

A recent extension of this strategy to other adenosine analog therapeutics, cladribine (CIA) and fludarabine (FIU) (Figure 4B), was reported (34). *In vitro* studies of CIADP and CIATP interactions with human- α revealed α_6 formation. Further assessment of the hexameric structures and their relationship to cell cytotoxicity is an ongoing challenge. Collectively, the results in cells and *in vitro* with these adenosine inhibitors suggest a potential new way to target RNR: trapping α in an inhibited state with a small molecule.

Pleiotropic modes of cytotoxicity of F₂C and CIF.

With both F₂C and CIF, the mechanisms of cytotoxicity require nucleoside uptake and metabolism (64, 65, 77). As noted above, the diphosphates and triphosphates of F₂C and CIF inhibit RNR and DNA polymerases, respectively (60, 78), the latter by chain termination. The consequences of DNA inhibition involving both targets are DNA replication stress that manifests as stalled or collapsed DNA replication forks, DNA single or strand breaks, which can lead to cell cycle arrest, DNA repair or programmed cell death (64) (see Figure 13).

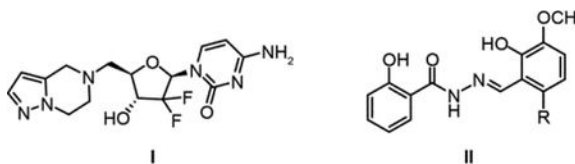
F₂CDP, a potent MBI of RNR, results in lower dNDP and consequently dNTP pools. Reduced dCTP, a feedback inhibitor of deoxycytidine kinase (3, Figure 13), results in

enhanced production of F₂CMP, leading to elevated levels of F₂CTP. The F₂CTP is then able to more effectively compete with lowered dNTPs pools to inhibit DNA synthesis. F₂C's broad spectrum of solid tumor inhibition, distinct from other nucleoside therapeutics such as araC, may be associated with the pleiotropic metabolic effects (Figure 13) resulting in its self-potentialization (69).

CIF is also phosphorylated by (3, Figure 13) and subsequently by distinct kinases to afford CIFDP and CIFTP. Its stability (due to F/Cl substitution) is increased relative to other adenosine analogs (CIA, FIU, Figure 4B) by its resistance to metabolism by purine nucleoside phosphorylase and adenosine deaminase. Down-stream consequences of DNA synthesis inhibition by F₂C and CIF are actively being pursued. F₂C is being investigated in combination with DNA damage response inhibitors of Chk1 (64, 68, 79, 80), with inhibitors of ATR in the same pathway (81), and with DNA repair enzyme inhibitors (65, 82). In addition, F₂C is often used in combination with cis-platin that enhances DNA damage and alters the downstream consequences. The ability to monitor the consequences of treatment with combinations of therapeutics using genomics, phospho-transcriptomics and metabolomics, have and will continue to aid in new approaches (65, 83).

Reversible C-site binders lacking phosphoryl groups.

Two compounds (**I** and **II**) have recently been reported to inhibit human RNR by binding reversibly to the C-site of α . In contrast to CIFDP and CIADP (Figure 4B), these small molecules lack the diphosphate moiety thought to be essential for substrate recognition. A 5'-substituted amine of F₂C (**I**), for example, is reported to inhibit RNR *in vitro* and *in vivo* (85). The unusual diphosphate binding site for NDP in α (no lysine, arginine or Mg²⁺) suggests that amine substitution might avoid issues associated with cellular uptake and phosphorylation (Figure 13). In a second case, Dealwis et al., reported molecules with a naphthyl salicyl hydrazone scaffold (**II**) that target the C-site of α and bind reversibly (86, 87). Decorating the scaffold, with an appropriately placed electrophilic moiety such as ClCH₂CO-(R''), could result in alkylation of one of the C-site cysteines, analogous to the mechanisms of covalent protein kinase inhibitors (88).



Reversible inhibitors that disrupt α/β subunit affinity.

The C-terminal tails (30 to 35 amino acids) of all β 2 subunits are disordered (Figure 2A) (14, 89–93), distinct, and predominantly responsible for subunit affinity (Figure 14). Early studies of Herpes simplex viruses (HSV-1, HSV-2), which encode for their own RNRs, provide an example of this approach (94, 95). Peptidomimetics of their tail were successfully developed that disrupted the α/β subunit interaction *in vitro* and in a murine ocular model of HSV-1 induced keratitis (96). The new structure of the *E. coli* α 2 β 2 (Figure 2D), which reveals for the first time the tail interaction (residues 341 to 375) with the α subunit (11), may suggest new approaches to disruption of this interface.

A second example of subunit disruption was reported by Yen's group (82, 97). They used the structure of human-p53 β 2 and computer modeling to identify a pocket in each β subunit close to the C-terminal tail but removed from the buried Fe³⁺₂-Y• cluster (Figure 1C) essential for β 2 stability. Virtual screening and additional experiments led to the identification of COH29 (Figure 14) that exhibited cytotoxicity to many of the NIH 60 cancer cell lines and caused S-phase cell cycle arrest. COH29 enhanced cytotoxicity of BRAC1 deficient HCC1937 cells. This report provides an example of DNA repair inhibition (98) (in this case genetically) that potentiated the effects of the RNR inhibitor COH29.

Biosynthesis and repair of the essential diferric-Y• cofactor of Ia RNRs: targeting the β 2 cofactor.

Whereas CIF and F₂C target α and the α/β subunits of RNR, respectively, hydroxyurea (HU) and triapine (3-AP, a thiosemicarbazone) (Figure 14) target reduction of the essential Y• (83, 99, 100) cofactor in β 2 and/or interfere with cofactor assembly and/or its repair if the essential Y• gets reduced (Figure 1C). HU is used clinically, predominantly in combination with other therapeutics (65), although recent studies suggest that RNR is not a key target of its cytotoxicity (99, 101, 102). Triapine (3-AP) continues to be examined in clinical trials, but has not yet been approved for clinical use (83, 100). Although the upstream target of both these compounds is RNR, the downstream pathways that lead to cytotoxicity are pleiotropic and distinct in different organisms. Herein we focus on HU and 3-AP inhibition of RNR *in vitro* and in the early stage of cell culture where cell viability remains high. Even under these conditions, their detailed mechanism(s) of RNR inhibition require further exploration.

Background for metallo-cluster metabolism.

The class Ia RNRs require a Fe³⁺₂-Y• cofactor in β 2 to initiate NDP reduction in α 2 with activity being directly proportional to the concentration of Y• (Figure 1C and Figure 3). The $t_{1/2}$ of the Y• in the cluster of different Ia β 2s is variable, ranging from 4 days in *E. coli* at 4° C to 30 min in humans at 37 °C. In addition, recombinant expression of β from different organisms results in variable amounts of active cofactor (0 to 1 Fe³⁺₂-Y•/ β 2) (6, 103). In general, therefore, the β 2 cofactor must be loaded by self-assembly using Fe²⁺ and O₂ with variable outcomes (6, 104). In the past two decades, the importance of biosynthetic pathways has been established for FeS cluster cofactor assembly that, in turn, has been linked to mono- and dinuclear non-heme iron cofactor formation including the RNR cofactor (105). Although much remains to be learned, genetic studies in *E. coli* and *S. cerevisiae*, and biochemical studies *in vitro* on these Ia β 2s, have suggested that there are pathways not only for cofactor biosynthesis, but also for its maintenance, and activity regulation (Figure 15). Our general model for Fe³⁺₂-Y• cofactor biosynthesis indicates the requirement for a chaperone protein(s) (106) to alter the apo- β 2 conformation for optimized Fe²⁺ loading, an Fe²⁺ carrier protein or small molecule that delivers Fe²⁺ to apo- β 2, and a reducing equivalent delivery mechanism required for cluster assembly with O₂ as the oxidant (107). Studies *in vivo* in *E. coli* (108) and *S. cerevisiae* (109) reveal that cluster assembly can yield β 2 with each β subunit having 2 Fe²⁺ and 1 Y•, that is, quantitative loading. *In vitro* however, *E. coli* β 2, loading gives rise to 66% of active cofactor and 33% of inactive diferric

cluster with no $Y\bullet$. In both *in vivo* and *in vitro* loading, the activity of RNR per $Y\bullet$ is the same, suggesting identical cofactor structures.

Hydroxyurea (HU).

HU (Figure 14) has been studied since the 1960s. Based on EPR analysis of prokaryotic and eukaryotic cells or of purified $\beta 2$ with a self-assembled $Fe^{3+}_2-Y\bullet$, HU treatment results in reduction of the $Y\bullet$ to YO. *In vitro*, the iron cluster of human $\beta 2$ is also reduced (Fe^{2+}_2-YO), whereas in *E. coli* it remains in the Fe^{3+} state (Fe^{3+}_2-YO). HU reduction of $\beta 2$ alone is slow ($0.45 M^{-1} s^{-1}$) and there is no evidence for its binding to either *E. coli* or human- $\beta 2$ (107, 110, 111). The chemical mechanism of $Y\bullet$ reduction and the structure of the resulting cluster remain unknown (112). Studies by the Sjöberg lab *in vitro* have shown that HU mediated loss of RNR activity is potentiated ten-fold by complexation of $\beta 2$ with $\alpha 2$, substrate and effector (113). This result led to their suggestion that its reduction of $Y_{122}\bullet$ is not direct, but instead might be trapping a “transient” pathway radical at the α/β subunit interface (Figure 3). Studies on the reduction by HU of the $Mn^{4+}-Fe^{3+}-\beta 2$ cofactor in the *C. trachomatis* Ic RNR (Figure 1C), an $Fe^{3+}_2-Y\bullet$ surrogate, were also interpreted to suggest that HU intercepts a pathway radical at the α/β interface (112). Furthermore, $Mn^{4+}-Fe^{3+}-\beta 2$ in the presence of $\alpha 2$, CDP, and ATP is reduced by HU to a $Mn^{3+}-Fe^{3+}$ cluster with half-sites reactivity involving a fast phase and a slow phase, with apparent saturation by HU for the fast phase. These studies support HU binding and targeting of the radical transfer pathway (112, 114). The consequences of the HU reduced cofactor state in *E. coli* and mammalian cells are still unclear; however, since the proteins identified in *S. cerevisiae* for $\beta 2$ cofactor biosynthesis and maintenance are also found in mammalian cells (107), $Y\bullet$ regeneration is one possible fate (maintenance pathway, Figure 15) and requires further investigation.

RNR inhibition by HU blocks DNA replication. Two papers have suggested that cytotoxicity from extended HU exposure of *E. coli* (100) or *S. cerevisiae* (102) cells is linked to reactive oxygen species (such as $HO\bullet$) mediated damage. Vernis et al. showed that HU resistance in *S. cerevisiae* led to enhanced production of the cytosolic FeS cluster biosynthetic machinery including Dre2/Tah18 (102). We have shown the importance of these two proteins in the assembly of the $\beta 2$ cofactor in *S. cerevisiae* (107).

Triapine.

Triapine (3-AP, Figure 14) has been extensively investigated since its introduction in the 1990's and its cytotoxic effects have inspired the synthesis of many additional thiosemicarbazones. However, studies on these analogs reveal that the mechanism of cytotoxicity changes with structure. The complexity arises from their distinct abilities to bind Fe^{2+} and Fe^{3+} (also Cu^{2+} and Zn^{2+} , not discussed) and the resultant ligand field imposed iron redox chemistry (100). The results reported by different groups (115, 116) in different mammalian cell lines, primarily at late stages of 3-AP treatment have thus made it challenging to compare and evaluate the outcomes between the different studies.

Our recent studies in cell culture in the “early” stages of 3-AP treatment are summarized and provide a framework for thinking about the issues and evaluation of their potential as therapeutics that target $\beta 2$ (115). Three mammalian cell lines (K565, COS-1 and HU

resistant TA3) treated with 3-AP and analyzed by whole cell EPR, revealed loss of the RNR $Y\bullet$ and assays of the corresponding cell lysates revealed loss of RNR activity. Immunoprecipitation of $\beta 2$ from ^{55}Fe treated and non-treated cells revealed similar iron content. These and additional studies suggested that the $Y\bullet$ loss is the major mode of RNR inhibition with iron loading remaining unchanged. Although the oxidation state of the bound iron is unknown, we know from *in vitro* studies that the Fe^{2+} loaded $\beta 2$ can assemble rapidly into the native $\text{Fe}^{3+}_2\text{-}Y\bullet$ cofactor, consistent with a maintenance pathway (Figure 15, green). Our model is that Fe^{2+} -(3-AP) is the active species involved in $\beta 2$ inhibition and that in the continued presence of $\text{Fe}^{2+}/\text{Fe}^{3+}$, RNR is susceptible to Fe^{2+} -(3-AP) inhibition by direct $Y\bullet$ reduction. Recent studies by Gräslund et al. using $[^3\text{H}]$ -3-AP and a docking model of 3-AP to mouse $\beta 2$, resulted in the proposal of a specific 3-AP binding site (116). However, neither 3-AP or Fe^{2+} -(3-AP) binding to $\beta 2$ has been observed. In our opinion, the mechanism of action of these compounds requires further study. Finally, our studies at early times subsequent to 3-AP treatment, in contrast with latter stage studies of others, indicate that reactive oxygen species are not responsible for RNR activity loss.

From the above discussion, how 3-AP and HU inhibit RNR and the relationship between their RNR inhibition and cell cytotoxicity still remain a mystery. Although interference with cluster assembly/maintenance might yield effective therapeutics, better understanding of the biology of $\text{Fe}^{3+}_2\text{-}Y\bullet$ pathways is required. The recent discovery, however, of $\text{Mn}^{3+}_2\text{-}Y\bullet$ cofactors in $\beta 2$ of Ib RNRs (Figure 1C) and the identification of a NrdI- $\beta 2$ interaction essential for oxidant delivery ($\text{O}_2\bullet^-$) for active cofactor formation (Figure 15) (6, 117), suggests that disruption of this protein/protein interface could provide proof of principle for targeting cofactor pathways in pathogenic bacteria. The link between the Ia $\text{Fe}^{3+}_2\text{-}Y\bullet$ pathway, iron homeostasis and oxidative stress will make selective targeting difficult. However, for pathogenic organisms with Mn and or Mn/Fe clusters (Figure 1C Ib–Id), interference with cluster assembly, may well provide a new therapeutic target.

References

1. Hofer A, Crona M, Logan DT, Sjöberg BM. 2012 DNA building blocks: keeping control of manufacture. *Crit. Rev. Biochem. Mol. Biol* 47: 50–63 [PubMed: 22050358]
2. Guarino E, Salguero I, Kearsley SE. 2014 Cellular regulation of ribonucleotide reductase in eukaryotes. *Semin. Cell Dev. Biol* 30: 97–103 [PubMed: 24704278]
3. Aye Y, Li M, Long MJC, Weiss RS. 2014 Ribonucleotide reductase and cancer: biological mechanisms and targeted therapies. *Oncogene* 34: 2011–21 [PubMed: 24909171]
4. Le TM, Poddar S, Capri JR, Abt ER, Kim W, et al. 2017 ATR inhibition facilitates targeting of leukemia dependence on convergent nucleotide biosynthetic pathways. *Nat. Commun* 8: 241 [PubMed: 28808226]
5. Licht S, Stubbe J. 1999 Mechanistic investigations of ribonucleotide reductases. *Compr. Nat. Prod. Chem* 5: 163–203
6. Cotruvo JA, Stubbe J. 2011 Class I ribonucleotide reductases: metallocofactor assembly and repair *in vitro* and *in vivo*. *Annu. Rev. Biochem* 80: 733–767 [PubMed: 21456967]
7. Minnihan EC, Nocera DG, Stubbe J. 2013 Reversible, long-range radical transfer in *E. coli* class Ia ribonucleotide reductase. *Acc. Chem. Res* 46: 2524–35 [PubMed: 23730940]
8. Fairman JW, Wijerathna SR, Ahmad MF, Xu H, Nakano R, et al. 2011 Structural basis for allosteric regulation of human ribonucleotide reductase by nucleotide-induced oligomerization. *Nat. Struct. Mol. Biol* 18: 316–22 [PubMed: 21336276]

9. Bennati M, Weber A, Antonic J, Perlstein DL, Robblee JH, Stubbe J. 2003 Pulsed ELDOR spectroscopy measured the distance between the two tyrosyl radicals in the R2 subunit of the *E. coli* ribonucleotide reductase. *J. Am. Chem. Soc* 125: 14988–9 [PubMed: 14653724]
10. Seyedsayamdost MR, Chan CTY, Mugnaini V, Stubbe J, Bennati M. 2007 PELDOR spectroscopy with DOPA- β 2 and NH₂Y- α 2s: distance measurements between residues involved in the radical propagation pathway of *E. coli* ribonucleotide reductase. *J. Am. Chem. Soc* 129: 15748–49 [PubMed: 18047343]
11. Kang G 2019 submitted. Massachusetts Institute of Technology, Cambridge, Massachusetts
12. Zimanyi CM, Chen PY, Kang G, Funk MA, Drennan CL. 2016 Molecular basis for allosteric specificity regulation in class Ia ribonucleotide reductase from *Escherichia coli*. *eLIFE* 5: e07141 [PubMed: 26754917]
13. Uhlin U, Eklund H. 1994 Structure of ribonucleotide reductase protein R1. *Nature* 370: 533–39 [PubMed: 8052308]
14. Eklund H, Uhlin U, Färnegårdh M, Logan DT, Nordlund P. 2001 Structure and function of the radical enzyme ribonucleotide reductase. *Prog. Biophys. Mol. Biol* 77: 177–268 [PubMed: 11796141]
15. Nordlund P, Sjöberg BM, Eklund H. 1990 Three-dimensional structure of the free radical protein of ribonucleotide reductase. *Nature* 345: 593–8 [PubMed: 2190093]
16. Stubbe J 1998 Ribonucleotide reductases in the twenty-first century. *Proc. Natl. Acad. Sci. U.S.A* 95: 2723–24 [PubMed: 9501154]
17. Stubbe J, Seyedsayamdost MR. 2019 Discovery of a new class I ribonucleotide reductase with an essential DOPA radical and NO metal as an initiator of long-range radical transfer. *Biochemistry* 58: 435–37 [PubMed: 30586288]
18. Srinivas V, Lebrette H, Lundin D, Kutin Y, Sahlin M, et al. 2018 Metal-free ribonucleotide reduction powered by a DOPA radical in *Mycoplasma* pathogens. *Nature* 563: 416–20 [PubMed: 30429545]
19. Blaesi EJ, Palowitch GM, Hu K, Kim AJ, Rose HR, et al. 2018 Metal-free class Ie ribonucleotide reductase from pathogens initiates catalysis with a tyrosine-derived dihydroxyphenylalanine radical. *Proc. Natl. Acad. Sci. U.S.A* 115: 10022–27 [PubMed: 30224458]
20. Jordan A, Reichard P. 1998 Ribonucleotide reductases. *Annu. Rev. Biochem* 67: 71–98 [PubMed: 9759483]
21. Nordlund P, Reichard P. 2006 Ribonucleotide reductases. *Annu. Rev. Biochem* 75: 681–706 [PubMed: 16756507]
22. Ge J, Yu G, Ator MA, Stubbe J. 2003 Pre-steady-state and steady-state kinetic analysis of *E. coli* class I ribonucleotide reductase. *Biochemistry* 42: 10071–83 [PubMed: 12939135]
23. Ravichandran KR, Taguchi AT, Wei Y, Nocera DG, Stubbe J. 2016 A >200 meV uphill thermodynamic landscape for radical transport in *E. coli* ribonucleotide reductase determined using fluorotyrosine-substituted enzymes. *J. Am. Chem. Soc* 138: 13706–16 [PubMed: 28068088]
24. Ravichandran KR, Zong AB, Taguchi AT, Nocera DG, Stubbe J, Tommos C. 2017 Formal reduction potentials of difluorotyrosine and trifluorotyrosine protein residues: defining the thermodynamics of multistep radical transfer. *J. Am. Chem. Soc* 139: 2994–3004 [PubMed: 28171730]
25. Minnihan EC, Ando N, Brignole EJ, Olshansky L, Chittuluru J, et al. 2013 Generation of a stable, aminotyrosyl radical-induced α 2 β 2 complex of *Escherichia coli* class Ia ribonucleotide reductase. *Proc. Natl. Acad. Sci. U.S.A* 110: 3835–40 [PubMed: 23431160]
26. Yokoyama K, Smith AA, Corzilius B, Griffin RG, Stubbe J. 2011 Equilibration of tyrosyl radicals (Y356•, Y731•, Y730•) in the radical propagation pathway of the *Escherichia coli* class Ia ribonucleotide reductase. *J. Am. Chem. Soc* 133: 18420–32 [PubMed: 21967342]
27. Brignole EJ, Tsai K-L, Chittuluru J, Li H, Aye Y, et al. 2018 3.3-Å resolution cryo-EM structure of human ribonucleotide reductase with substrate and allosteric regulators bound. *Elife* 7: e31502 [PubMed: 29460780]
28. Ando N, Li H, Brignole EJ, Thompson S, McLaughlin MI, et al. 2016 Allosteric inhibition of human ribonucleotide reductase by dATP entails the stabilization of a hexamer. *Biochemistry* 55: 373–81 [PubMed: 26727048]

29. Ando N, Brignole EJ, Zimanyi CM, Funk MA, Yokoyama K, et al. 2011 Structural interconversions modulate activity of *Escherichia coli* ribonucleotide reductase. Proc. Natl. Acad. Sci. U.S.A 108: 21046–51 [PubMed: 22160671]
30. Zimanyi CM, Ando N, Brignole EJ, Asturias FJ, Stubbe J, Drennan CL. 2012 Tangled up in knots: structures of inactivated forms of *E. coli* class Ia ribonucleotide reductase. Structure 20: 1374–83 [PubMed: 22727814]
31. Chen PY, Funk MA, Brignole EJ, Drennan CL. 2018 Disruption of an oligomeric interface prevents allosteric inhibition of *Escherichia coli* class Ia ribonucleotide reductase. J. Biol. Chem 293: 10404–12 [PubMed: 29700111]
32. Ahluwalia D, Bienstock RJ, Schaaper RM. 2012 Novel mutator mutants of *E. coli* nrdAB ribonucleotide reductase: Insight into allosteric regulation and control of mutation rates. DNA Repair 11: 480–87 [PubMed: 22417940]
33. Aye Y, Brignole EJ, Long MJ, Chittuluru J, Drennan CL, et al. 2012 Clofarabine targets the large subunit (alpha) of human ribonucleotide reductase in live cells by assembly into persistent hexamers. Chem. Biol 19: 799–805 [PubMed: 22840768]
34. Wisitpitthaya S, Zhao Y, Long MJC, Li M, Fletcher EA, et al. 2016 Cladribine and fludarabine nucleotides induce distinct hexamers defining a common mode of reversible RNR inhibition. ACS Chem. Biol 11: 2021–32 [PubMed: 27159113]
35. Fu Y, Long MJC, Wisitpitthaya S, Inayat H, Pierpont TM, et al. 2018 Nuclear RNR-alpha antagonizes cell proliferation by directly inhibiting ZRANB3. Nat. Chem. Biol 14: 943–54 [PubMed: 30150681]
36. Lin Q, Parker MJ, Taguchi AT, Ravichandran K, Kim A, et al. 2017 Glutamate 52-β at the α/β subunit interface of *Escherichia coli* class Ia ribonucleotide reductase is essential for conformational gating of radical transfer. J. Biol. Chem 292: 9229–39 [PubMed: 28377505]
37. Erickson HK. 2001 Kinetics in the pre-steady state of the formation of cystines in ribonucleoside diphosphate reductase: evidence for an asymmetric complex. Biochemistry 40: 9631–37 [PubMed: 11583163]
38. Lou M, Liu Q, Ren GP, Zeng JL, Xiang XP, et al. 2017 Physical interaction between human ribonucleotide reductase large subunit and thioredoxin increases colorectal cancer malignancy. J. Biol. Chem 292: 9136–49 [PubMed: 28411237]
39. Makhlynets O, Boal AK, Rhodes DV, Kitten T, Rosenzweig AC, Stubbe J. 2014 Streptococcus sanguinis class Ib ribonucleotide reductase: high activity with both iron and manganese cofactors and structural insights. J. Biol. Chem 289: 6259–72 [PubMed: 24381172]
40. Lu J, Holmgren A. 2014 The thioredoxin antioxidant system. Free Rad. Biol. Med 66: 75–87 [PubMed: 23899494]
41. Parker MJ, Stubbe J. 2014 *Bacillus subtilis* class Ib ribonucleotide reductase: high activity and dynamic subunit interactions. Biochemistry 53: 766–76 [PubMed: 24401092]
42. Ravichandran KR, Olshansky L, Nocera DG, Stubbe J. Subunit interaction dynamics of the *E. coli* class Ia ribonucleotide reductase. BioRxiv submitted
43. Stubbe J, van der Donk WA. 1998 Protein radicals in enzyme catalysis. Chem. Rev 98: 705–62 [PubMed: 11848913]
44. Stubbe J, Ackles D. 1980 On the mechanism of ribonucleoside diphosphate reductase from *Escherichia coli*. Evidence for 3'-C-H bond cleavage. J. Biol. Chem 255: 8027–30 [PubMed: 6997288]
45. Lenz R, Giese B. 1997 Studies on the mechanism of ribonucleotide reductases. J. Am. Chem. Soc 119: 2784–94
46. Licht SS, Booker S, Stubbe J. 1999 Studies on the catalysis of carbon-cobalt bond homolysis by ribonucleoside triphosphate reductase: evidence for concerted carbon-cobalt bond homolysis and thiyl radical formation. Biochemistry 38: 1221–33 [PubMed: 9930982]
47. Licht S, Gerfen GJ, Stubbe J. 1996 Thiyl radicals in ribonucleotide reductases. Science 271: 477–81 [PubMed: 8560260]
48. Lawrence CC, Bennati M, Obias HV, Bar G, Griffin RG, Stubbe J. 1999 High-field EPR detection of a disulfide radical anion in the reduction of cytidine 5'-diphosphate by the E₄₄₁Q-R1 mutant of

- Escherichia coli* ribonucleotide reductase. Proc. Natl. Acad. Sci. U.S.A 96: 8979–84 [PubMed: 10430881]
49. Pizano AA, Lutterman DA, Holder PG, Teets TS, Stubbe J, Nocera DG. 2011 Photo-ribonucleotide reductase beta2 by selective cysteine labeling with a radical phototrigger. Proc. Natl. Acad. Sci. U.S.A 109: 39–43 [PubMed: 22171005]
 50. Chang MCY, Yee CS, Stubbe J, Nocera DG. 2004 Turning on ribonucleotide reductase by light-initiated amino acid radical generation. Proc. Natl. Acad. Sci. U.S.A 101: 6882–87 [PubMed: 15123822]
 51. Olshansky L, Pizano AA, Wei Y, Stubbe J, Nocera DG. 2014 Kinetics of hydrogen atom abstraction from substrate by an active site thiyl radical in ribonucleotide reductase. J. Am. Chem. Soc 136: 16210–6 [PubMed: 25353063]
 52. Licht SS, Lawrence CC, Stubbe J. 1999 Class II ribonucleotide reductases catalyze carbon-cobalt bond reformation on every turnover. J. Am. Chem. Soc 121: 7463–68
 53. Stubbe J, van der Donk WA. 1995 Ribonucleotide reductases: Radical enzymes with suicidal tendencies. Chem. Biol 2: 793–801 [PubMed: 8807812]
 54. Thelander L, Larsson B, Hobbs J, Eckstein F. 1976 Active site of ribonucleoside diphosphate reductase from *Escherichia coli*. J. Biol. Chem 251: 1396–405
 55. van der Donk WA, Yu G, Silva DJ, Stubbe J, McCarthy JR, et al. 1996 Inactivation of Ribonucleotide Reductase by (E)-2'-Fluoromethylene-2'-deoxycytidine 5'-Diphosphate: A Paradigm for Nucleotide Mechanism-Based Inhibitors. Biochemistry 35: 8381–91 [PubMed: 8679596]
 56. Bitonti AJ, Dumont JA, Bush TL, Cashman EA, Cross-Doersen DE, et al. 1994 Regression of human breast tumor xenografts in response to (E)-2'-deoxy-2'-(fluoromethylene)cytidine, an inhibitor of ribonucleoside diphosphate reductase. Cancer Res 54: 1485–90 [PubMed: 8137252]
 57. Zhou Y, Achanta G, Pelicano H, Gandhi V, Plunkett W, Huang P. 2002 Action of (E)-2'-deoxy-2'-(fluoromethylene)cytidine on DNA metabolism: incorporation, excision, and cellular response. Mol. Pharmacol 61: 222–9 [PubMed: 11752224]
 58. Baker CH, Banzon J, Bollinger JM, Stubbe J, Samano V, et al. 1991 2'-Deoxy-2'-methylene-2'-deoxy-2',2'-difluorocytidine 5'-diphosphates: potent mechanism-based inhibitors of ribonucleotide reductase. J. Med. Chem 34: 1879–84 [PubMed: 2061926]
 59. Xie KC, Plunkett W. 1996 Deoxynucleotide pool depletion and sustained inhibition of ribonucleotide reductase and DNA synthesis after treatment of human lymphoblastoid cells with 2-chloro-9-(2-deoxy-2-fluoro-beta-D-arabinofuranosyl) adenine. Cancer Res 56: 3030–7 [PubMed: 8674058]
 60. Xie C, Plunkett W. 1995 Metabolism and actions of 2-chloro-9-(2-deoxy-2-fluoro-beta-D-arabinofuranosyl)-adenine in human lymphoblastoid cells. Cancer Res 55: 2847–52 [PubMed: 7540950]
 61. Aye Y, Stubbe J. 2011 Clofarabine 5'-di and -triphosphates inhibit human ribonucleotide reductase by altering the quaternary structure of its large subunit. Proc. Natl. Acad. Sci. U.S.A 108: 9815–20 [PubMed: 21628579]
 62. Fritscher J, Artin E, Wnuk S, Bar G, Robblee JH, et al. 2005 Structure of the nitrogencentered radical formed during inactivation of *E. coli* ribonucleotide reductase by 2'-azido-2'-deoxyuridine-5'-diphosphate: trapping of the 3'-ketonucleotide. J. Am. Chem. Soc 127: 7729–38 [PubMed: 15913363]
 63. Sjöberg BM, Gräslund A, Eckstein F. 1983 A substrate radical intermediate in the reaction between ribonucleotide reductase from *Escherichia coli* and 2'-azido-2'-deoxynucleoside diphosphates. J. Biol. Chem 258: 8060–7 [PubMed: 6305969]
 64. Ewald B, Sampath D, Plunkett W. 2008 Nucleoside analogs: molecular mechanisms signaling cell death. Oncogene 27: 6522–37 [PubMed: 18955977]
 65. Murai J 2017 Targeting DNA repair and replication stress in the treatment of ovarian cancer. Int. J. Clin. Oncol 22: 619–28 [PubMed: 28643177]
 66. Bonate PL, Arthaud L, Cantrell WR Jr., Stephenson K, Secrist JA, Weitman S. 2006 Discovery and development of clofarabine: a nucleoside analogue for treating cancer. Nat. Rev. Drug Discov 5: 855–63 [PubMed: 17016426]

67. Hertel LW, Boder GB, Kroin JS, Rinzel SM, Poore GA, Todd GC, Grindey GB 1990 Evaluation of the antitumor-activity of gemcitabine (2',2'-difluoro-2'-deoxycytidine). *Cancer Res* 50: 4417–22 [PubMed: 2364394]
68. Ewald B, Sampath D, Plunkett W. 2007 H2AX phosphorylation marks gemcitabine-induced stalled replication forks and their collapse upon S-phase checkpoint abrogation. *Mol. Cancer Ther* 6: 1239–48 [PubMed: 17406032]
69. Plunkett W, Huang P, Searcy CE, Gandhi V. 1996 Gemcitabine: preclinical pharmacology and mechanisms of action. *Semin. Oncol* 23: 3–15
70. van der Donk WA, Yu GX, Pérez L, Sanchez RJ, Stubbe J, Samano V, Robins MJ 1998 Detection of a new substrate-derived radical during inactivation of ribonucleotide reductase from *Escherichia coli* by gemcitabine 5'-diphosphate. *Biochemistry* 37: 6419–26 [PubMed: 9572859]
71. Artin E, Wang J, Lohman GJ, Yokoyama K, Yu G, et al. 2009 Insight into the mechanism of inactivation of ribonucleotide reductase by gemcitabine 5'-diphosphate in the presence or absence of reductant. *Biochemistry* 48: 11622–9 [PubMed: 19899770]
72. Wang J, Lohman GJ, Stubbe J. 2009 Mechanism of inactivation of human ribonucleotide reductase with p53R2 by gemcitabine 5'-diphosphate. *Biochemistry* 48: 11612–21 [PubMed: 19899807]
73. Chen Z, Zhou J, Zhang Y, Bepler G. 2011 Modulation of the ribonucleotide reductase M1-gemcitabine interaction *in vivo* by N-ethylmaleimide. *Biochem. Biophys. Res. Commun* 413: 383–8 [PubMed: 21893046]
74. Wang J, Lohman GJ, Stubbe J. 2007 Enhanced subunit interactions with gemcitabine-5'-diphosphate inhibit ribonucleotide reductases. *Proc. Natl. Acad. Sci. U.S.A* 104: 14324–9 [PubMed: 17726094]
75. Thomas WC, Brooks FP, Burnim AA, Bacik JP, Stubbe J, et al. 2019 Convergent allostery in ribonucleotide reductase. *Nat. Commun* 10: 2653 [PubMed: 31201319]
76. Ghanem H, Jabbour E, Faderl S, Ghandi V, Plunkett W, Kantarjian H. 2010 Clofarabine in leukemia. *Expert. Rev. Hematol* 3: 15–22 [PubMed: 21082931]
77. Wong A, Soo RA, Yong WP, Innocenti F. 2009 Clinical pharmacology and pharmacogenetics of gemcitabine. *Drug Metab. Rev* 41: 77–88 [PubMed: 19514966]
78. Xie C, Plunkett W. 1995 Metabolism and actions of 2-chloro-9-(2-deoxy-2-fluoro-beta-D-arabinofuranosyl)-adenine in human lymphoblastoid cells. *Cancer Res* 55: 2847–52 [PubMed: 7540950]
79. Warren NJH, Eastman A. 2019 Inhibition of checkpoint kinase 1 following gemcitabine-mediated S phase arrest results in CDC7- and CDK2-dependent replication catastrophe. *J. Biol. Chem* 294: 1763–78 [PubMed: 30573684]
80. Liu Y, Li Y, Wang X, Liu F, Gao P, et al. 2017 Gemcitabine and chk1 inhibitor AZD7762 synergistically suppress the growth of Lkb1-deficient lung adenocarcinoma. *Cancer Res* 77: 5068–76 [PubMed: 28754670]
81. Fordham SE, Blair HJ, Elstob CJ, Plummer R, Drew Y, et al. 2018 Inhibition of ATR acutely sensitizes acute myeloid leukemia cells to nucleoside analogs that target ribonucleotide reductase. *Blood Adv* 2: 1157–69 [PubMed: 29789314]
82. Chen YR, Tsou B, Hu S, Ma H, Liu X, et al. 2016 Autophagy induction causes a synthetic lethal sensitization to ribonucleotide reductase inhibition in breast cancer cells. *Oncotarget* 7: 1984–99 [PubMed: 26675256]
83. Mannargudi MB, Deb S. 2017 Clinical pharmacology and clinical trials of ribonucleotide reductase inhibitors: is it a viable cancer therapy? *J. Cancer Res. Clin. Oncol* 143: 1499–529 [PubMed: 28624910]
84. Long MJC, Van Hall-Beauvais A, Aye Y. 2019 The more the merrier: how homo-oligomerization alters the interactome and function of ribonucleotide reductase. *Curr. Opin. Chem. Biol* 54:10–8 [PubMed: 31734537]
85. Labroli MA, Dwyer MP, Shen R, Popovici-Muller J, Pu Q, et al. 2014 The identification of novel 5'-amino gemcitabine analogs as potent RRM1 inhibitors. *Bioorg. Med. Chem* 22: 2303–10 [PubMed: 24588962]
86. Misko TA, Liu YT, Harris ME, Oleinick NL, Pink J, et al. 2019 Structure-guided design of anti-cancer ribonucleotide reductase inhibitors. *J. Enz. Inhib. Med. Chem* 34: 438–50

87. Ahmad MF, Alam I, Huff SE, Pink J, Flanagan SA, et al. 2017 Potent competitive inhibition of human ribonucleotide reductase by a nonnucleoside small molecule. *Proc. Natl. Acad. Sci. U.S.A* 114: 8241–46 [PubMed: 28716944]
88. Backus KM, Cao J, Maddox SM. 2019 Opportunities and challenges for the development of covalent chemical immunomodulators. *Bioorg. Med. Chem* 27: 3421–39 [PubMed: 31204229]
89. Moss N, Beaulieu P, Duceppe JS, Ferland JM, Gauthier J, et al. 1995 Peptidomimetic inhibitors of herpes simplex virus ribonucleotide reductase: a new class of antiviral agents. *J. Med. Chem* 38: 3617–23 [PubMed: 7658449]
90. Climent I, Sjöberg BM, Huang CY. 1991 Carboxyl-terminal peptides as probes for *Escherichia coli* ribonucleotide reductase subunit interaction: kinetic analysis of inhibition studies. *Biochemistry* 30: 5164–71 [PubMed: 2036382]
91. Climent I, Sjöberg BM, Huang CY. 1992 Site-directed mutagenesis and deletion of the carboxyl terminus of *Escherichia coli* ribonucleotide reductase protein R2 - effects on catalytic activity and subunit interaction. *Biochemistry* 31: 4801–7 [PubMed: 1591241]
92. Xu H, Fairman JW, Wijerathna SR, Kreischer NR, LaMacchia J, et al. 2008 The structural basis for peptidomimetic inhibition of eukaryotic ribonucleotide reductase: a conformationally flexible pharmacophore. *J. Med. Chem* 51: 4653–9 [PubMed: 18610997]
93. Cooperman BS, Gao Y, Tan C, Kashlan OB, Kaur J. 2005 Peptide inhibitors of mammalian ribonucleotide reductase. *Adv. Enz. Reg* 45: 112–25
94. Cohen EA, Gaudreau P, Brazeau P, Langelier Y. 1986 Specific inhibition of herpesvirus ribonucleotide reductase by a nonapeptide derived from the carboxy terminus of subunit 2. *Nature* 321: 441–43 [PubMed: 3012360]
95. Dutia BM, Frame MC, Subak-Sharpe JH, Clark WN, Marsden HS. 1986 Specific inhibition of herpesvirus ribonucleotide reductase by synthetic peptides. *Nature* 321: 439–41 [PubMed: 3012359]
96. Liuzzi M, Déziel R, Moss N, Beaulieu P, Bonneau A-M, et al. 1994 A potent peptidomimetic inhibitor of HSV ribonucleotide reductase with antiviral activity *in vivo*. *Nature* 372: 695–98 [PubMed: 7990963]
97. Zhou B, Su L, Hu S, Hu W, Yip ML, et al. 2013 A small-molecule blocking ribonucleotide reductase holoenzyme formation inhibits cancer cell growth and overcomes drug resistance. *Cancer Res* 73: 6484–93 [PubMed: 24072748]
98. Chen MC, Zhou B, Zhang K, Yuan YC, Un F, et al. 2015 The novel ribonucleotide reductase inhibitor COH29 inhibits DNA repair *in vitro*. *Mol. Pharmacol* 87: 996–1005 [PubMed: 25814515]
99. Singh A, Xu YJ. 2016 The Cell Killing Mechanisms of Hydroxyurea. *Genes (Basel)* 7: 99
100. Heffeter P, Pape VF, Enyedy EA, Keppler BK, Szakacs G, Kowol CR. 2019 Anticancer thiosemicarbazones: chemical properties, interaction with iron metabolism, and resistance development. *Antiox. Redox Sig* 30: 1062–82
101. Davies BW, Kohanski MA, Simmons LA, Winkler JA, Collins JJ, Walker GC. 2009 Hydroxyurea induces hydroxyl radical-mediated cell death in *Escherichia coli*. *Mol. Cell* 36: 845–60 [PubMed: 20005847]
102. Huang ME, Facca C, Fatmi Z, Baille D, Benakli S, Vernis L. 2016 DNA replication inhibitor hydroxyurea alters Fe-S centers by producing reactive oxygen species *in vivo*. *Sci. Rep* 6: 29361 [PubMed: 27405729]
103. Stubbe J, Cotruvo JA. 2011 Control of metallation and active cofactor assembly in the class Ia and Ib ribonucleotide reductases: diiron or dimanganese? *Curr. Op. Chem. Bio* 15: 284–90
104. Atkin CL, Thelander L, Reichard P, Lang G. 1973 Iron and free radical in ribonucleotide reductase. Exchange of iron and Mössbauer spectroscopy of the protein B2 subunit of the *Escherichia coli* enzyme. *J. Biol. Chem* 248: 7464–72 [PubMed: 4355582]
105. Mühlhoff U, Molik S, Godoy JR, Uzarska MA, Richter N, et al. 2010 Cytosolic monothiol glutaredoxins function in intracellular iron sensing and trafficking via their bound iron-sulfur cluster. *Cell Metab* 12: 373–85 [PubMed: 20889129]
106. Sluder IT, Nitika, Knighton LE, Truman AW. 2018 The Hsp70 co-chaperone Ydj1/HDJ2 regulates ribonucleotide reductase activity. *PLoS Genet* 14: e1007462 [PubMed: 30452489]

107. Zhang Y, Li H, Zhang C, An X, Liu L, et al. 2014 Conserved electron donor complex Dre2-Tah18 is required for ribonucleotide reductase metallocofactor assembly and DNA synthesis. *Proc. Natl. Acad. Sci. U.S.A* 111: E1695–704 [PubMed: 24733891]
108. Hristova D, Wu CH, Jiang W, Krebs C, Stubbe J. 2008 Importance of the maintenance pathway in the regulation of the activity of *Escherichia coli* ribonucleotide reductase. *Biochemistry* 47: 3989–99 [PubMed: 18314964]
109. Ortigosa AD, Hristova D, Perlstein DL, Zhang Z, Huang M, Stubbe J. 2006 Determination of the *in vivo* stoichiometry of tyrosyl radical per $\beta\beta'$ in *Saccharomyces cerevisiae* ribonucleotide reductase. *Biochemistry* 45: 12282–94 [PubMed: 17014081]
110. Lassmann G, Thelander L, Gräslund A. 1992 EPR stopped-flow studies of the reaction of the tyrosyl radical of protein R2 from ribonucleotide reductase with hydroxyurea. *Biochem. Biophys. Res. Commun* 188: 879–87 [PubMed: 1332707]
111. Swarts JC, Aquino MA, Han JY, Lam KY, Sykes AG. 1995 Kinetic studies on the reduction of the tyrosyl radical of the R2 subunit of *E. coli* ribonucleotide reductase. *Biochim. Biophys. Acta* 1247: 215–24 [PubMed: 7696311]
112. Jiang W, Xie J, Varano PT, Krebs C, Bollinger JM. 2010 Two distinct mechanisms of inactivation of the class Ic ribonucleotide reductase from *Chlamydia trachomatis* by hydroxyurea: implications for the protein gating of intersubunit electron transfer. *Biochemistry* 49: 5340–49 [PubMed: 20462199]
113. Karlsson M, Sahlin M, Sjöberg BM. 1992 *Escherichia coli* ribonucleotide reductase. Radical susceptibility to hydroxyurea is dependent on the regulatory state of the enzyme. *J. Biol. Chem* 267: 12622–6 [PubMed: 1618767]
114. Bollinger JM Jr., Jiang W, Green MT, Krebs C. 2008 The manganese(IV)/iron(III) cofactor of *Chlamydia trachomatis* ribonucleotide reductase: structure, assembly, radical initiation, and evolution. *Curr. Opin. Struct. Biol* 18: 650–7 [PubMed: 19046875]
115. Aye Y, Long MJ, Stubbe J. 2012 Mechanistic studies of semicarbazone triapine targeting human ribonucleotide reductase *in vitro* and in mammalian cells: tyrosyl radical quenching not involving reactive oxygen species. *J. Biol. Chem* 287: 35768–78 [PubMed: 22915594]
116. Popovi -Bijeli A, Kowol CR, Lind ME, Luo J, Himo F, et al. 2011 Ribonucleotide reductase inhibition by metal complexes of Triapine (3-aminopyridine-2-carboxaldehyde thiosemicarbazone): a combined experimental and theoretical study. *J. Inorg. Biochem* 105: 1422–31 [PubMed: 21955844]
117. Boal AK, Cotruvo JA Jr., Stubbe J, Rosenzweig AC. 2010 Structural basis for activation of class Ib ribonucleotide reductase. *Science* 329: 1526–30 [PubMed: 20688982]
118. Parker MJ, Maggiolo AO, Thomas WC, Kim A, Meisburger SP, et al. 2018 An endogenous dAMP ligand in *Bacillus subtilis* class Ib RNR promotes assembly of a noncanonical dimer for regulation by dATP. *Proc. Natl. Acad. Sci. U.S.A* 115: E4594–E603 [PubMed: 29712847]
119. Johansson R, Jonna Venkateswara R, Kumar R, Nayeri N, Lundin D, et al. 2016 Structural mechanism of allosteric activity regulation in a ribonucleotide reductase with double ATP cones. *Structure* 24: 906–17 [PubMed: 27133024]

Summary points

1. The quaternary structures of the class Ia RNR α subunit are nucleotide-dependent and distinct. α structures detected to date are: $\alpha 2$, non-canonical $\alpha 2$ (118), $\alpha 4$, $\alpha 6$, and fibrils (27, 75).
2. dATP-inhibited RNR structures include $\alpha 6$ (human), $\alpha 4\beta 4$ (*E. coli*), $\alpha 4$ (*P. aeruginosa*) (119), and a double helical fibril of canonical and non-canonical $\alpha 2$ s (Ib, *B. subtilis*) (75).
3. dATP inhibited states appear to interfere with the radical transfer pathway and thyl radical formation by preventing $\beta 2$ from achieving a productive $\alpha 2\beta 2$ complex.
4. CIFDP (CIFTP) bind to human-RNR and form conformationally “stable” $\alpha 6$ state(s), even subsequent to their dissociation.
5. N_3 NDP and F_2 CDP are mechanism-based inhibitors of class Ia RNRs with one inhibitor/ $\alpha 2$ in the $\alpha 2\beta 2$ complex, half-sites reactivity; half-sites reactivity.
6. Incorporation of unnatural amino acids ($F_3Y_{122}\bullet$ or $NO_2Y_{122}\bullet$ - β or NH_2Y_{356} - β , NH_2Y_{731} or NH_2Y_{730} - α) and incubation with the second subunit, substrate, and effector, trap radicals within the pathway and increase α/β subunit affinity.
7. The reaction of $F_3Y_{122}\bullet$ /E52Q- $\beta 2$ with $\alpha 2$, substrate, and effector, results in an asymmetric, active, and kinetically trapped $\alpha 2\beta 2$ complex, whose structure has been determined by cryo-EM.

Future studies

Continued studies of the structure, dynamics, and biology of RNRs

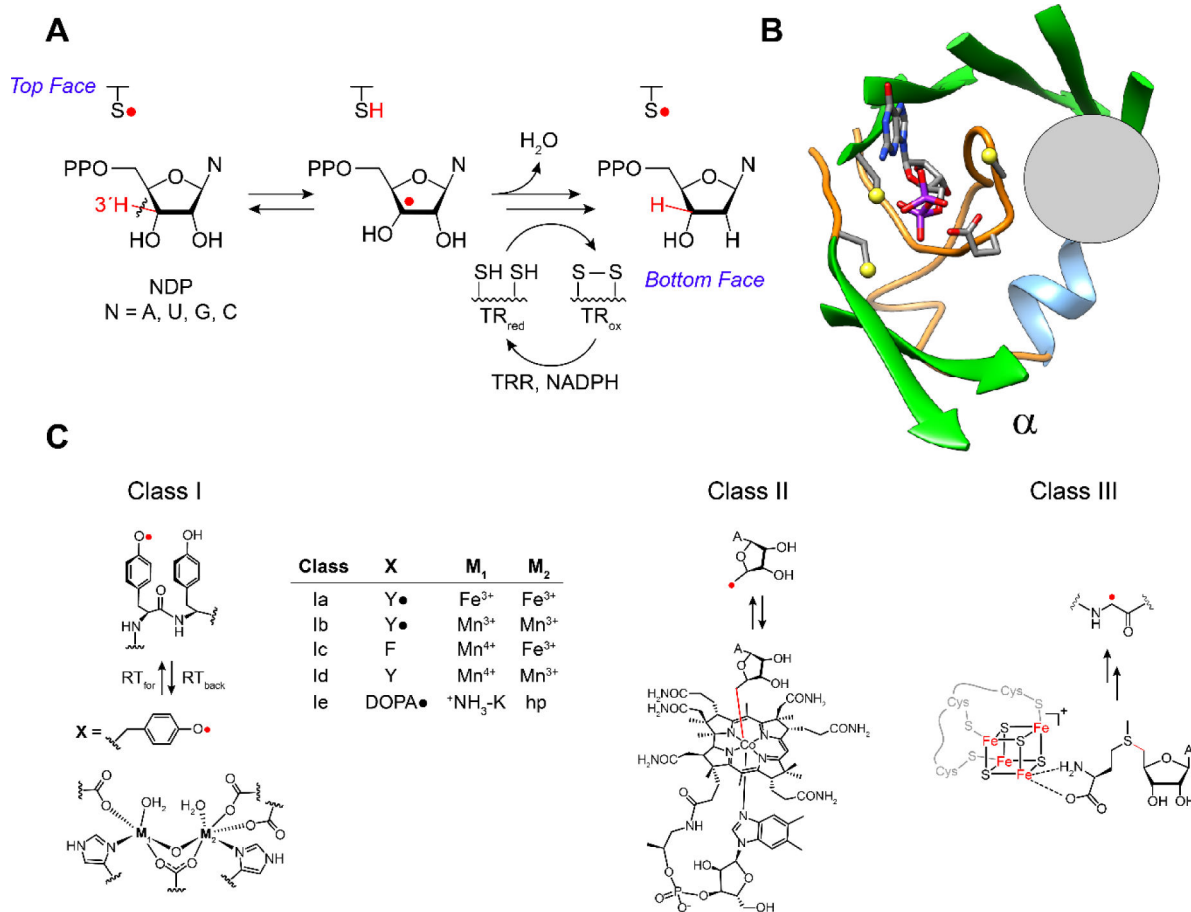
1. Trapping of additional $\alpha 2\beta 2$ complexes of RNR with mechanism-based inhibitors, and unnatural amino acid-mutants may provide distinct and higher resolution structures.
2. The active form of a mutant *E. coli* Ia RNR has been shown by cryo-EM analysis to be an asymmetric and dynamic $\alpha 2\beta 2$. The relationship of this structure to the wt enzyme and the structure of the human active complex remain to be established.

New ways to target RNRs

1. Identification of small molecules that can trap human and bacterial RNRs in distinct inhibited quaternary structures.
2. The discovery of biosynthetic pathways for dimetallo- $Y\bullet$ cluster assembly in Ia and Ib RNRs suggest that targeting the metal center formation, such as disruption of NrdI-NrdF interaction in the assembly of the class Ib, $Mn^{3+}_2-Y\bullet$ cofactor, might be possible.
3. The omics revolution (proteomics, phosphomics, transcriptomics) and a refined understanding of nucleotide metabolism are providing new insight into RNR regulation. This knowledge will lead to combination chemotherapies using RNR inhibitors in conjunction with inhibitors of downstream signaling pathways.

BOX 1 The model (Figure 7) encompasses weak, dynamic, subunit interactions that change with subunit and dNTP concentrations by altering RNR quaternary structure and activity. The assays/issues for the *E. coli* RNR are described in BioRxiv (42) and are essential for development of *in vitro* and *in vivo* high throughput screens for RNR inhibitors. The same issues are likely to be encountered, to different extents, with other Ia and Ib RNRs.

BOX2 Moonlighting function of α . A recent report (35) and review (84) provide support for a “moonlighting” function for α , independent of its ability with β to make dNDPs in the cytosol of the cell. Using a C→S mutant that inactivates formation of $-S^{\bullet}$ in α (Figure 1A), a small amount of α was detected in the nucleus of the cell in an α_6 state. Yeast two hybrid experiments with cDNA from HELA cells revealed that α interacts with ZRANB3, a protein that forms a complex with PCNA, the sliding clamp that together with DNA polymerase promotes DNA synthesis in non-stressed cells. Nuclear localized α inhibits the interaction of ZRANB3 with PCNA resulting in inhibition of DNA synthesis. This study potentially provides an explanation for the tumor suppressor activity reported for α (3).

**Figure 1.**

A RNRs catalyze the conversion of nucleoside di- or triphosphates, ND(T)Ps, to deoxynucleoside di- or triphosphate, dND(T)Ps. **B** The reduction occurs in the active site in subunit α composed of a 10 stranded β barrel with three cysteines and the conserved placement of the oxidant (gray circle, panel B) involved in thiyl radical formation ($-S^\bullet$, top face in **A**) that initiates NDP reduction. The bottom face thiols in **A** deliver the reducing equivalents and themselves become oxidized. **C** The oxidants are distinct among the RNR classes (I, II and III) represented here by a gray circle that is juxtaposed with the thiyl radical loop. Substrate and four essential residues, including the three essential cysteines and E₄₄₁, are shown as sticks. **C** The class Ia RNRs use a diferric-tyrosyl radical (Y^\bullet) cofactor ($M_1, M_2 = Fe^{3+}$) that is located in subunit β (left, bottom) to regenerate a radical species in the active site in subunit α . The oxidation occurs over a distance of ~ 33 Å by long range radical transfer to first generate a Y^\bullet in subunit α (under the gray circle), and second generate $-S^\bullet$ on an adjacent cysteine (top face in **A**). In other class I RNRs (Ib-Ie) the oxidation also occurs by long range radical transfer across α and β , but involves distinct metallo-oxidants (X, M_1, M_2). In the case of the class II and III RNRs the oxidants, the 5'-deoxyadenosyl radical generated from adenosylcobalamin (class II) and the glycyl radical (class III) generated from S-adenosylmethionine and an FeS cluster, are located adjacent to the cysteine to be oxidized (gray circle). A = adenine base.

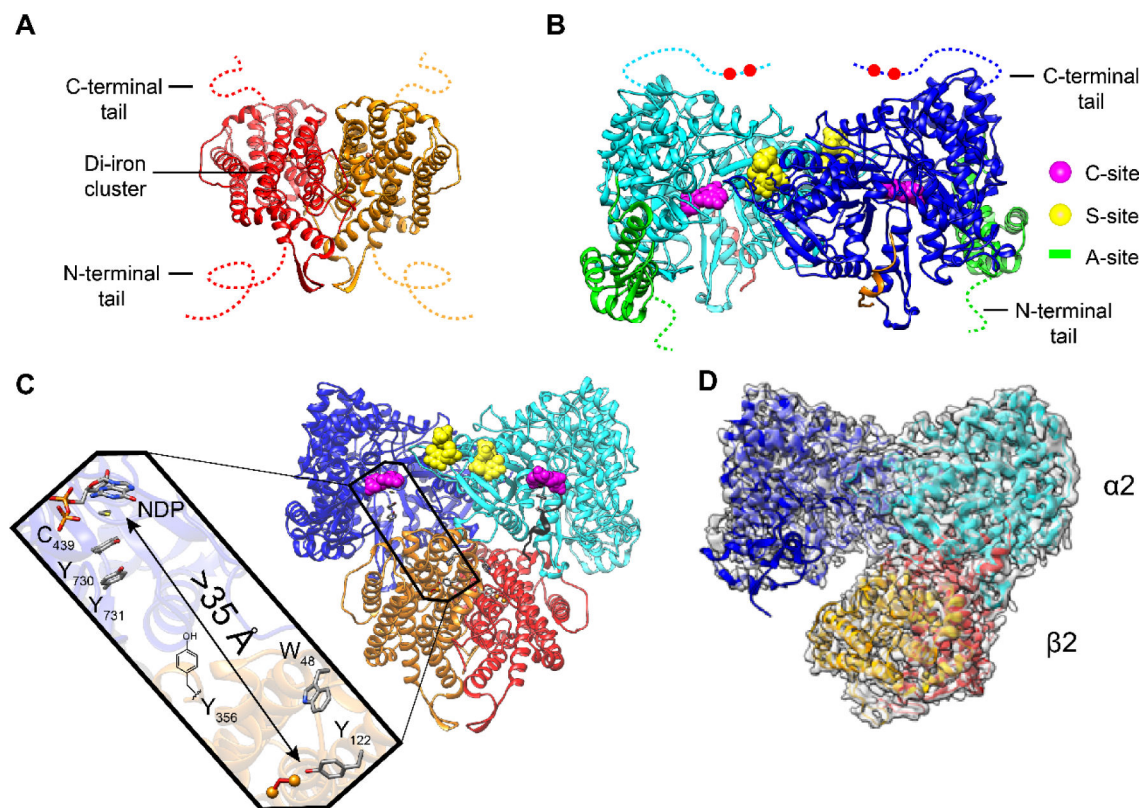


Figure 2.

Structural models of class Ia RNR from *E. coli*. X-ray structures of **A** $\beta 2$ (15), **B** $\alpha 2$ (13), **C** the Eklund docking model of $\alpha 2\beta 2$ (13), and **D** a cryo-EM structure of an active $\alpha 2\beta 2$ with two mutations in $\beta 2$: F₃Y₁₂₂/E52Q (11). **A** $\beta 2$, a homodimer in red/orange with disordered C-terminal tail residues (dashed lines 341–375 *E. coli*). **B** $\alpha 2$, a homodimer in light and dark blue with disordered C-terminal tail residues (dashed lines 737–761) that houses the two cysteines (red balls) which re-reduce the active site disulfide formed on NDP reduction (Figure 1A). $\alpha 2$ also houses the A-site (activity site or cone domain) that binds ATP (that activates RNR) or dATP (that inactivates RNR) in green; the C-site (catalytic site that binds CDP, UDP, GDP, and ADP) in magenta; the S-site (specificity site that binds the effectors dATP, ATP, TTP dGTP) in yellow. **C** Docking model of $\alpha 2\beta 2$ with the long-range radical transfer pathway (left) (14). Shown also is a peptide in gray (residues 360–375 of $\beta 2$) proposed to represent the tail of $\beta 2$ responsible for $\alpha 2$ binding. **D** Asymmetric complex formed when F₃Y₁₂₂/E52Q- $\beta 2$, interacts with $\alpha 2$, GDP, and TTP. 3.6-Å resolution cryo-EM density shown in transparent gray. This structure of the active $\alpha 2\beta 2$ can be compared with the symmetric docking model in **C**.

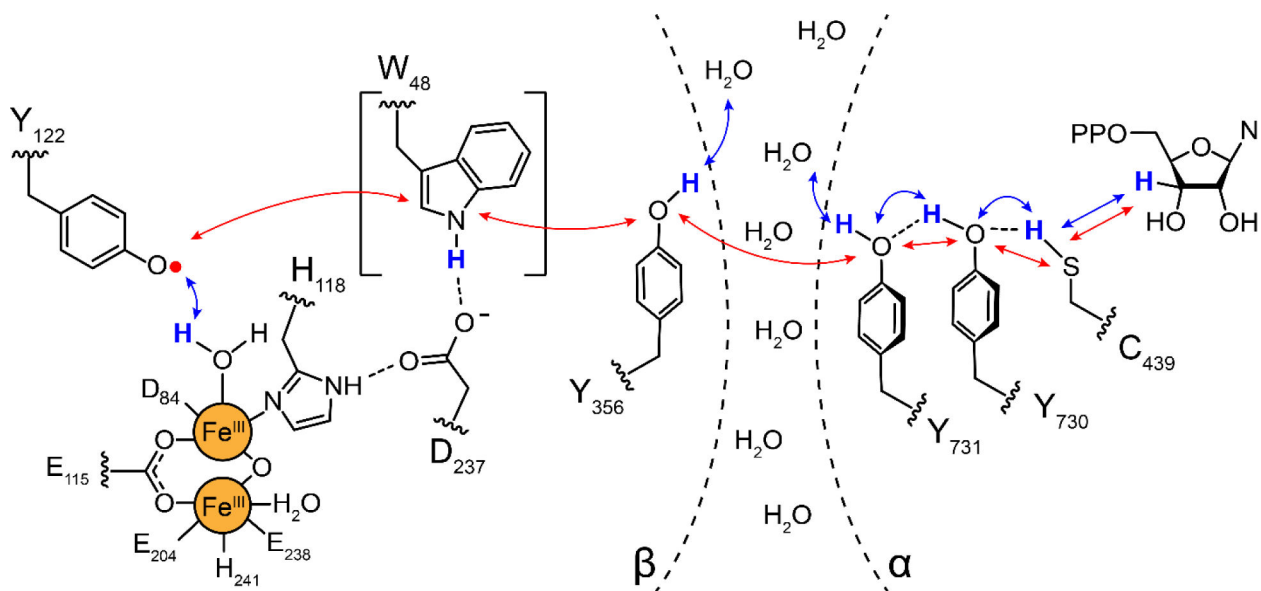


Figure 3. Proposed radical transfer pathway in Ia RNRs (*E. coli* numbering) within the $\alpha_2\beta_2$ complex. Binding of substrate and allosteric effector (not shown) to α_2 , triggers radical transfer from the Y_{122}^\bullet of the Fe^{3+}_2 - Y_{122}^\bullet cofactor in β , through three transient Y^\bullet s (356- β across the subunit interface to 731- α and 730- α). The Y_{730}^\bullet - α (under the gray circle in Figure 1B) then oxidizes the active site cysteine to a $-S^\bullet$ that initiates NDP reduction (Figure 1A). Subsequent to dNDP formation, the Y_{122}^\bullet is regenerated by reverse radical transfer. W_{48} - β is bracketed as its role in the pathway has not been established. Each step in the pathway is proposed to involve distinct proton (H^+ , blue arrows) coupled electron (e^- , red arrows) transfer (PCET) steps indicated by blue and red arrows (7).

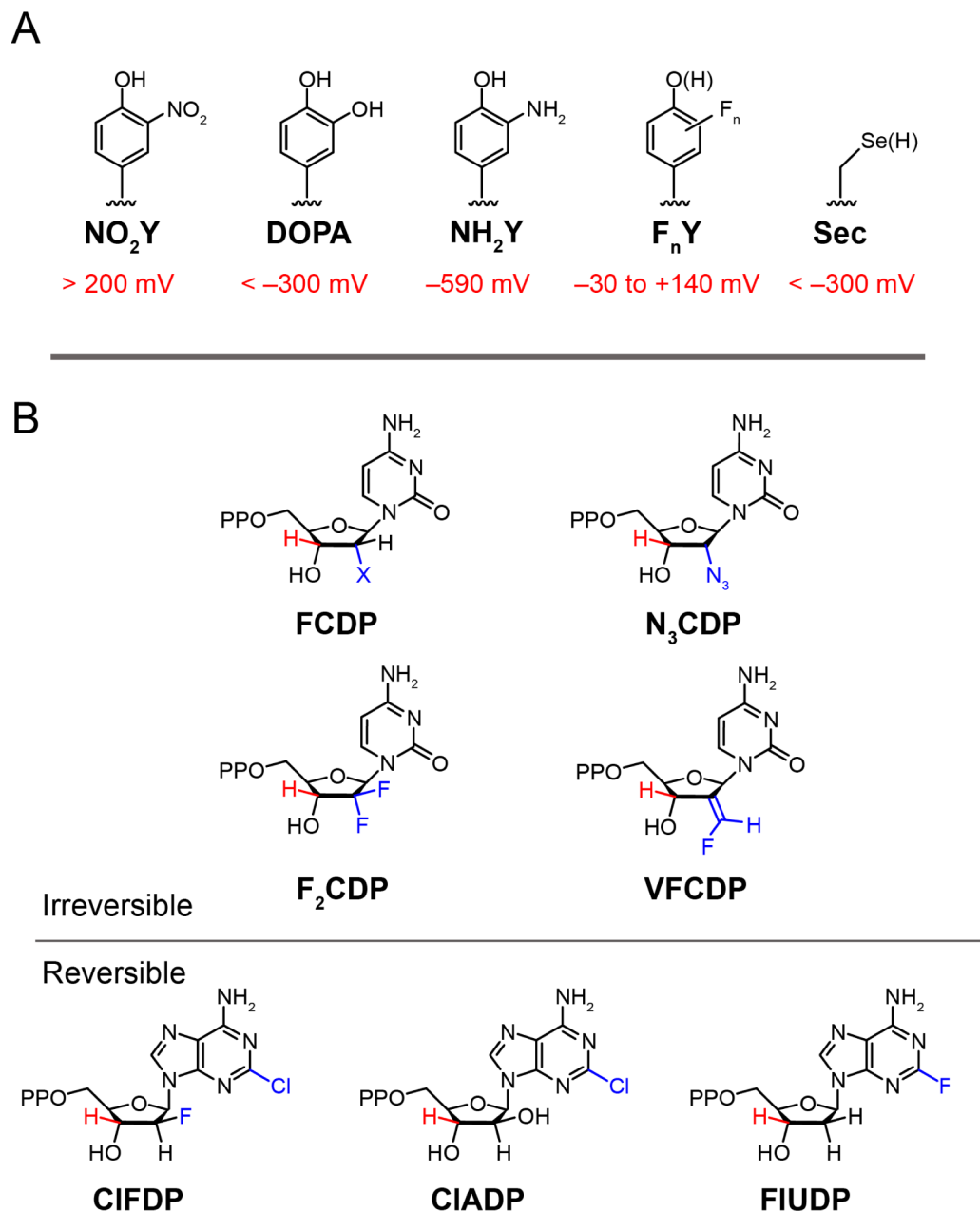


Figure 4. Structures of unnatural amino acids and nucleotide analogs used to study class Ia RNRs. **A** Unnatural amino acids that have been site-specifically incorporated in place of the tyrosines or cysteine within the radical transfer pathway (Figure 3) and their reduction potentials vs. tyrosine for NO₂Y, DOPA, NH₂Y, F_nYs and vs. cysteine for selenocysteine (Sec) at pH 7 (24). 3-Aminotyrosine (NH₂Y) is 590 mV easier to oxidize than Y. Fluorinated Ys (F_nY where n = 2 or 3) have allowed for tuning of the reduction potential over 170 mV depending on the number of Fs and their substitution pattern. **B** Nucleoside 5'-diphosphate are irreversible and reversible inhibitors of RNR. The irreversible inhibitors are mechanism based as the 3' C-H bond (red) of the inhibitor must be cleaved as with the normal substrate

(Figure 1A), before distinct radical chemistry in each case occurs that causes enzyme inactivation.

Author Manuscript

Author Manuscript

Author Manuscript

Author Manuscript

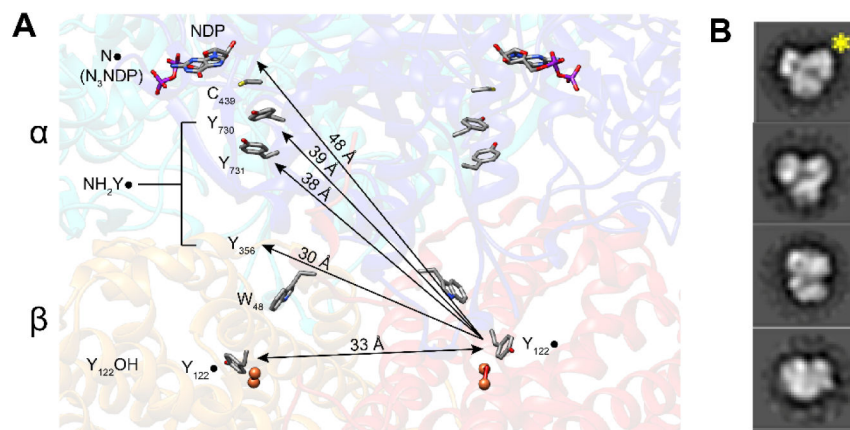


Figure 5. Support for the Eklund docking model (Figure 2C). **A** PELDOR spectroscopy used to measure distances between $Y_{122}\bullet$ in the unreacted α/β pair (right) and the trapped radicals ($NH_2Y\bullet$ or $N\bullet$) in the reactive α/β pair where Y_{122} is reduced (YOH, left). **B** Representative negative stain EM 2D class averages of the structures of the $NH_2Y_{730}\bullet$ trapped in $\alpha_2\beta_2$ complex (25). The view with the yellow star resembles the Eklund docking model shown in Figure 2C.

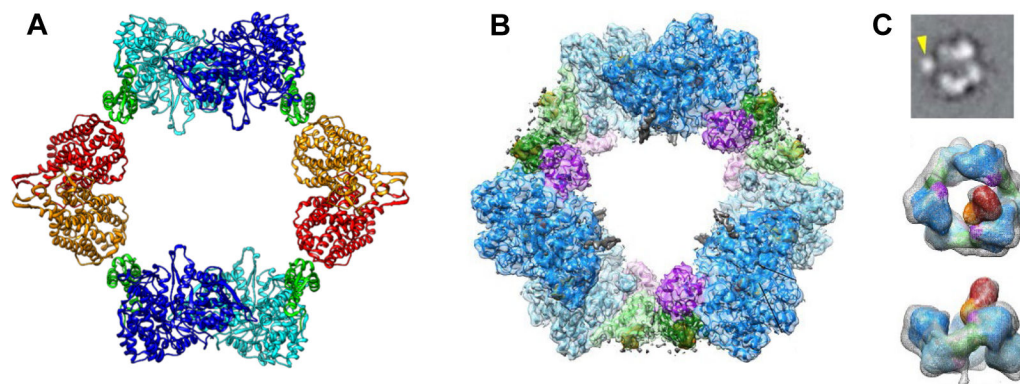
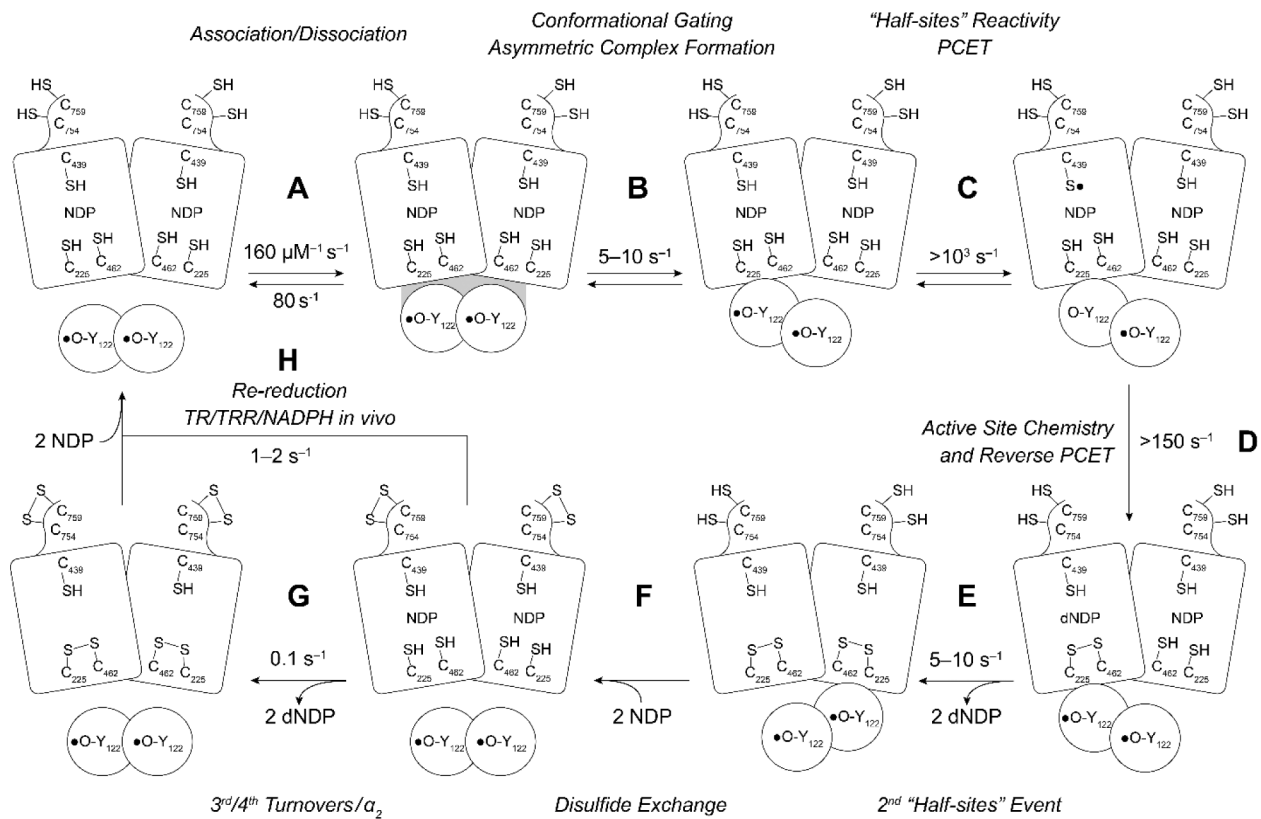


Figure 6.

Structures of dATP inhibited states of class Ia RNRs. **A** X-ray structure of dATP inhibited *E. coli* class Ia RNR (29) is an $\alpha_4\beta_4$ ring structure with a hole in the middle, composed of alternating α_2 (light and dark blue with the cone domains in green) and β_2 (orange and red) subunits. Note the importance of the cone domain in the α/β interaction. **B** Cryo-EM structure of dATP inhibited human class Ia RNR (27) is a hexameric α_6 ring with a hole in the middle. A subunits are in light blue and dark blue with cone domain in light and dark green and a three-helix insertion in purple (residues 638–681). Note the importance of the cone domain in the α/α interactions. **C** Cryo-EM structure of α/β (1:1) clofarabine triphosphate (CIFTP) inhibited human class Ia RNR (27). Top panel is a representative cryo-EM 2D class average image generated from α , β and clofarabine triphosphate (CIFTP) that shows β (arrow) interacting with α . The middle and bottom panels are two views of the 3D reconstruction of the same data set. The bottom is rotated 90° from the middle image. Only a fraction of the α_6 rings in these images have a single and variably positioned β .

**Figure 7.**

Resetting RNR for single and multiple turnovers. The model assumes a 1:1 α to β ratio, that Y_{122}^\bullet is distributed equally between each β , and that the wt- $\alpha_2\beta_2$ complex is asymmetric. In the absence of external reductants, 2 dCDPs are generated at 2 (substrate only) to 5–10 s^{-1} (substrate and effector) that arise from chemistry at each α of α_2 (step E). Steps B and E are rate-limiting and conformationally gated. In an assay in the absence of an external reductant, two additional dCDPs are formed at 0.1 s^{-1} (step G). In the presence of an external reductant such as thioredoxin (TR) and TR reductase (TRR), under steady state conditions, step H becomes rate-limiting.

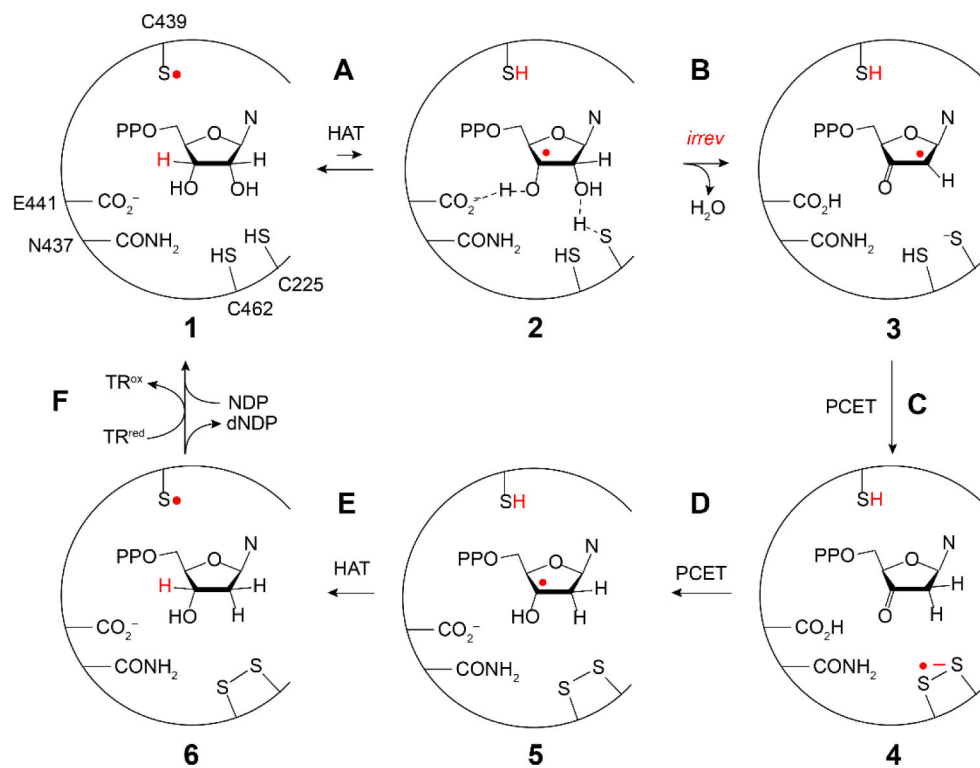


Figure 8. Mechanism of $-S\cdot$ mediated NDP reduction by most RNRs (5). Steps **A–F** are the proposed steps in the reaction and **1–6** represent the active site participants in each step. Note that steps **A**, **C**, **D**, and **E** involve either hydrogen atom transfer (HAT) or proton coupled electron transfer (PCET) processes.

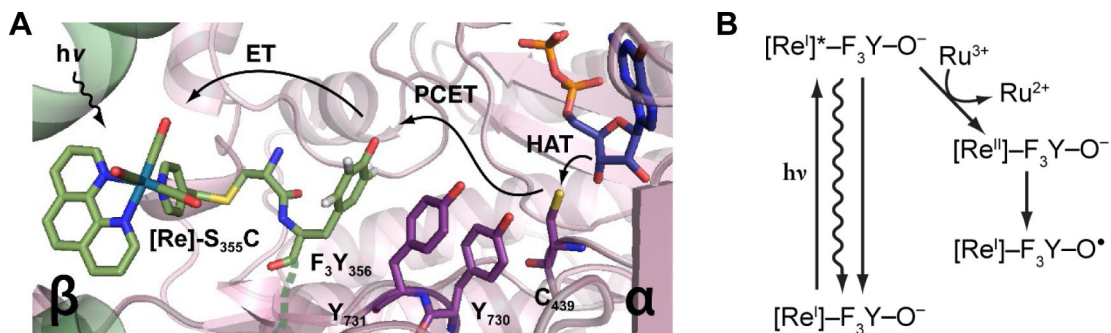


Figure 9.

Use of photoRNPs to unmask rates of chemical steps. **A** Schematic of photo β 2 with rehenium photooxidant [Re] attached covalently to C₃₅₅ and Y₁₂₂OH- β 2 (that is, Y₁₂₂[•] is reduced) complexed with CDP, ATP, and α 2 (49). In the case shown, Y₃₅₆ in β is replaced with the unnatural amino acid 2,3,5-F₃Y₃₅₆. (Figure 4). **B** Light initiates the reaction and the presence of the flash quencher, Ru(NH₃)₆Cl₃, prevents charge recombination (left) and generates [Re^{II}]-F₃Y-O⁻ (right), that rapidly drives 2,3,5-F₃Y₃₅₆ oxidation to the 3,5-F₃Y₃₅₆[•] that initiates chemistry within α 2. Different mechanisms of oxidation shown are electron transfer (ET), PCET, proton coupled electron transfer, and HAT, hydrogen atom transfer.

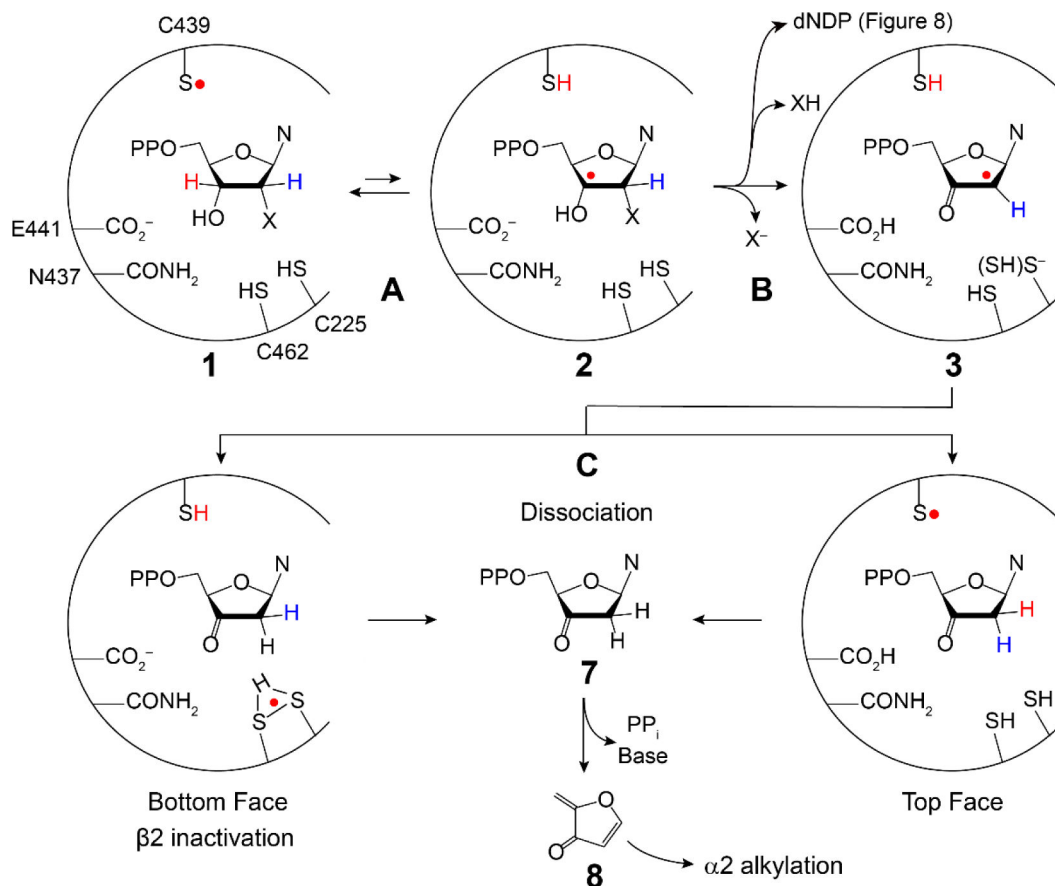


Figure 10.

Generic mechanism for 2' X-dNDP ($X = \text{F}, \text{Cl}, \text{N}_3, \text{F}_2$ (Figure 4)) mechanism-based inhibition of RNRs with loss of X^- in step **B** (43, 53). **3** is formed with bottom face protonation states of the thiols unknown, which can be reduced from the top face by SH to produce **7** (right) or the bottom face to produce **7** (left) which dissociates from the active site and then decomposes to generate the products (PP_i , Base and **8**). **8** can alkylate the α subunit. Alternatively, if in conversion of **2** to **3** (step **B**), XH is eliminated, and the normal product dNDP is formed.

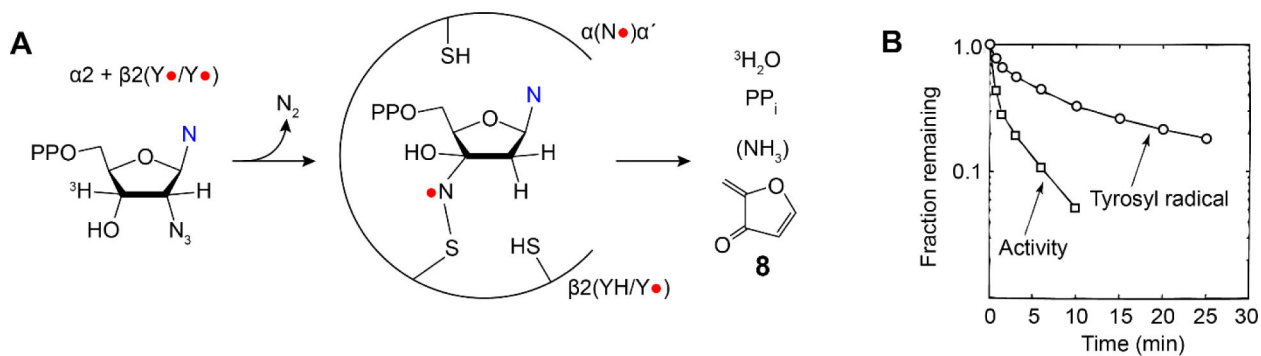
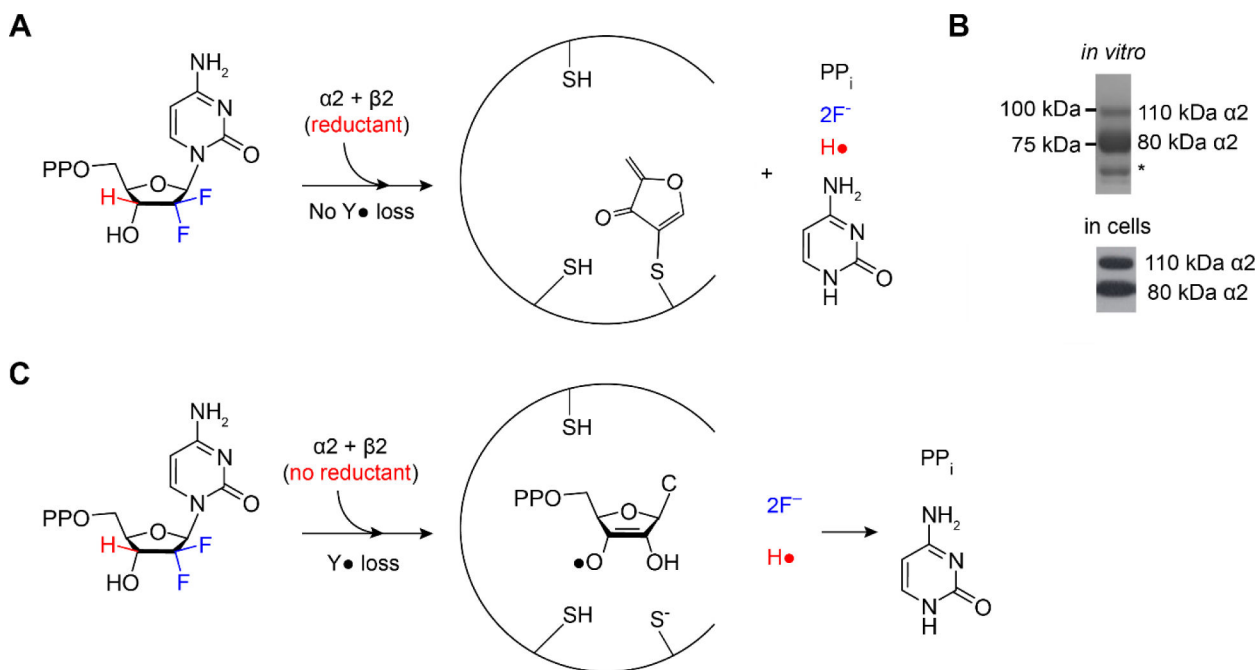


Figure 11.

N_3NDP (Figure 4B) is a potent inhibitor of all Ia RNRs (62,63). Studies of this inhibitor provided a glimpse of unprecedented chemistry associated with reactive radical species in an active site cavity and the challenges associated with radical structure elucidation. It also provided the first evidence for half-sites reactivity.

**Figure 12.**

Products of RNR inhibition experiments depend on whether reductant is used. **A** F_2CDP is a MBI of *E. coli* and human RNRs in the presence of reductant (protein TR or dithiothreitol) *in vitro* (70–72), **B** in cell lines (73), and **C** in the absence of reductant *in vitro*. **A** and **C** show the products produced during RNR inactivation. **B** shows SDS-PAGE of RNR from studies *in vitro* and cell lysate without boiling after incubation with F_2CDP (*in vitro*) or F_2C (in cells). Wt- α (80 kDa, C), migrates as 110 kDa.

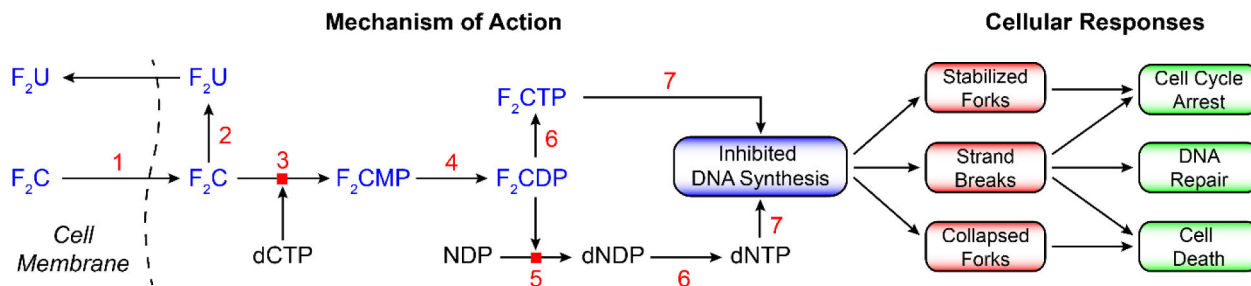


Figure 13.

A general scheme for metabolism of nucleosides using F_2C as an example (64). F_2C and CIF therapeutics require cellular uptake and phosphorylation to the appropriate state recognized by target enzymes. The former is mediated by nucleoside transporters ENT1, ENT2, and CNT [1]. Once inside the cell, both F_2C and CIF are phosphorylated to the monophosphate by deoxycytidine kinase [3] and subsequently to the di and triphosphates by cellular kinases [4 and 6]. Deoxycytidine kinase has unusual specificity in that it phosphorylates both pyrimidines and purines. The concentrations of the monophosphates are in general $>$ than the triphosphates \gg than the diphosphates, are cell type distinct, and influence therapeutic outcomes. [5] is RNR, [7] is DNA polymerase, and [2] is cytidine deaminase.

Peptide inhibition of α/β interactions

Organism	C-terminal sequence β
HSV	YAGAVVNDL
Mammalian	NSFTLDADF
<i>E. coli</i>	YLVGQIDSEVDTDDL SNFQL
<i>M. tuberculosis</i>	VTEDDDWDF
<i>S. cerevisiae</i>	AGAFTFNEDF

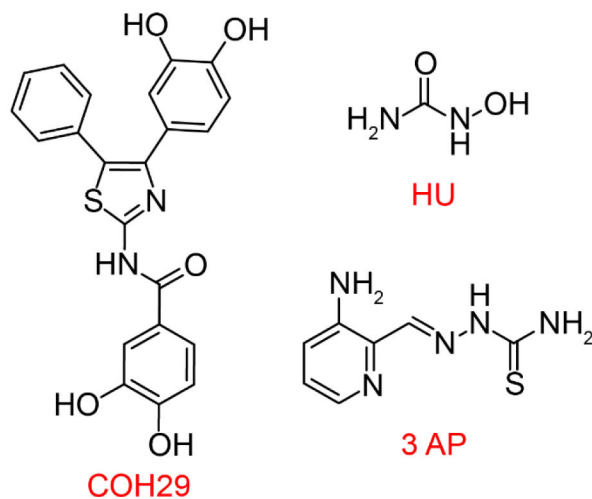


Figure 14.

Targeting the α/β interface of active RNR to prevent active complex formation with peptidomimetics and COH29. Targeting formation and repair of $\text{Me}_2^{3+}\text{-Y}\cdot$ (Me is Fe)-cofactor of β_2 with HU and triapine, 3-AP.

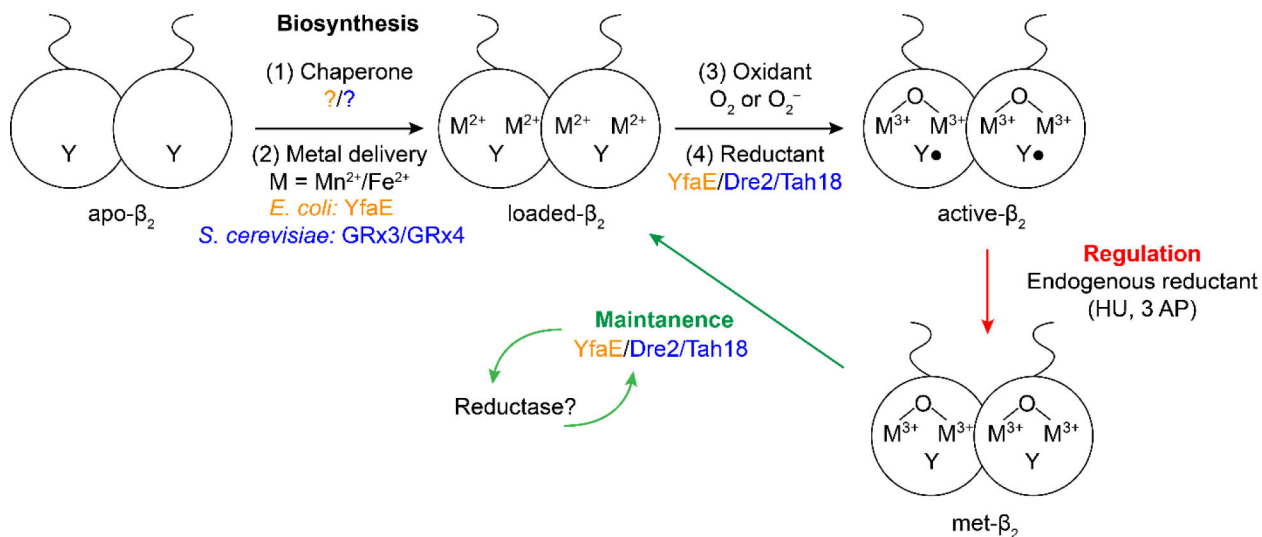


Figure 15. Model for $\text{Me}_2^{3+}\text{-Y}\cdot$ (Me is Fe or Mn) cofactor biosynthesis (black), maintenance (green) and regulation (red) with factors identified from *E. coli* in orange and from *S. cerevisiae* in blue (6). *S. cerevisiae* counterparts are found in humans. Regulation can occur by endogenous reductants or by therapeutics such as HU and triapine (Figure 14).

Table 1.

Pathway radicals trapped in *E. coli* class Ia RNR by site-specifically incorporating unnatural amino acids or reaction with N₃UDP; PELDOR distances ($< \pm 1 \text{ \AA}$) are given in last column. ● corresponds to forward RT and ● to reverse RT, as indicated by the direction of the arrows on the pathway shown below the table.

α	β	Y ₁₂₂	Y ₃₅₆	Y ₇₃₁	Y ₇₃₀	C ₄₃₉	NDP	Y ₁₂₂ [•] -X [•] distance (Å)
WT	WT	●●	-	-	-	-	-	33
WT	DOPA ₃₅₆	-	●	-	-	-	-	30
WT	NH ₂ Y ₃₅₆	-	●	-	-	-	-	30
Y ₇₃₁ F	F ₃ Y ₁₂₂	-	●	-	-	-	-	30
NH ₂ Y ₇₃₁	WT	-	-	●	-	-	-	38
NH ₂ Y ₇₃₁ /R ₄₁₁ A	WT	-	-	●	-	-	-	35
NH ₂ Y ₇₃₀	WT	-	-	-	●	-	-	39
WT	WT	-	-	-	-	-	N ₃ UDP●	48
WT	F ₃ Y ₁₂₂	-	●	-	-	-	-	30
WT	NO ₂ Y ₁₂₂	-	●	-	-	-	-	30